Aster repulsion drives local ordering in an active system

Jorge de-Carvalho[1], Sham Tlili[2,#], Lars Hufnagel[3], Timothy E. Saunders[2,4,5,*], Ivo A. Telley[1,*]

[1] Instituto Gulbenkian de Ciência, Fundação Calouste Gulbenkian, Oeiras, Portugal
[2] Mechanobiology Institute, National University of Singapore, Singapore
[3] European Molecular Biology Laboratory, Heidelberg, Germany
[4] Department of Biological Sciences, National University of Singapore, Singapore
[5] Institute of Molecular and Cellular Biology, A*Star, Proteos, Singapore
[*] For correspondence: dbsste@nus.edu and itelley@igc.gulbenkian.pt
[#] Present address: Aix-Marseille Université | AMU · Institut de Biologie du Développement de Marseille-Luminy (UMR 7288 IBDML)

Abstract:

Biological systems are a form of active matter, that often undergo rapid changes in their material state, *e.g.* liquid to solid transitions. Yet, such systems often also display remarkably ordered structures. It remains an open question as to how local ordering occurs within active systems. Here, we utilise the rapid early development of *Drosophila melanogaster* embryos to uncover the mechanisms driving short-ranged order. During syncytial stage, nuclei synchronously divide (within a single cell defined by the ellipsoidal eggshell) for nine cycles after which most of the nuclei reach the cell cortex. Despite the rapid nuclear division and repositioning, the spatial pattern of nuclei at the cortex is highly regular. Such precision is important for subsequent cellularisation and morphological transformations. We utilise *ex vivo* explants and mutant embryos to reveal that microtubule asters ensure the regular distribution and maintenance of nuclear positions in the embryo. For large networks of nuclei, such as in the embryo, we predict – and experimentally verify – the formation of force chains. The *ex vivo* extracts enabled us to deduce the force potential between single asters. We use this to predict how the nuclear division axis orientation in small *ex vivo* systems depend on aster number. Finally, we demonstrate that, upon nucleus removal from the cortex, microtubule force potentials can reorient subsequent nuclear divisions to minimise the size of pattern defects. Overall, we show that short-ranged microtubule-mediated repulsive interactions between asters can drive ordering within an active system.

Keywords

Centrosome, cytoskeleton, force chains, packing, ex vivo, microtubules, syncytium

Introduction

Proliferation of the genome is a cornerstone of early development in all animals, generally achieved by cell division. Almost all insects first segregate genome copies into hundreds of nuclei (syncytium) and only at a specific nuclear density transform the single cell into a tissue[1]. The distribution and separation of nuclei in syncytia typically display surprising positional uniformity[2–4]. This uniformity is likely required for precise gene patterning and fate determination[5]. How the embryo controls internuclear distance so robustly has been a decades-long topic of debate[6–12].

In *Drosophila melanogaster*, early nuclear divisions are meta-synchronous, whereby nuclei gradually fill the inner cellular space until, nine division cycles or ~80 minutes post-fertilisation, 300–400 of them arrive at the cell cortex[13]. The nuclei are subsequently embedded within a two-dimensional topology near the cortex of the ellipsoidal embryo, where they undergo four more rounds of division to generate ~6000 nuclei[14] prior to cellularisation. Some nuclei do not reach the cell cortex, resulting in the final number after 13 divisions at the cortex being less than 8192 (2^{13}). The spatiotemporal synchronisation of nuclear divisions is governed by a reaction-diffusion process emerging from nuclei[4]. Furthermore, global nuclear positioning in the early embryo is crucial for synchronisation[9].

Microtubule dynamics is critical for nuclear migration to the cortex at nuclear cycle (n.c.) 9 and for their regular distribution upon arrival[15–17]. Nuclei are embedded in a regular matrix that either pulls or pushes them apart, leading to precise internuclear distances. In interphase of the cell cycle, microtubules are organised in radial arrays called 'asters', which are nucleated and organised by the centrosome[18–20]. The centrosome acts as the main microtubule organising centre (MTOC) and promotes polymerisation and focusing of microtubules[21]. Two asters are linked to each nucleus, being functional elements of the bipolar spindle during mitosis. Asters are required for nuclear separation following chromosome segregation in the embryo[22]. Embryos lacking core centrosomal components do not regularly distribute nuclei and abort development after a few division cycles[23–25]. Conversely, embryos that do not form actin caps and membrane furrowing, which are the precursor of uninuclear cell formation and are thought to help separate nuclei at the cortex, still show regular nuclear distribution at n.c. 10 and 11 [10]. The causality and the mode of mechanical separation during and after nuclear division remains an open problem, primarily due to limited visualisation in living samples and the growing mechanical complexity during development.

Here, by exploiting embryonic explants[26], which reduces complexity, and a cell cycle regulation mutant[27,28] to uncouple microtubule organisation from nuclear division, we determine how microtubule interactions spatially organise nuclei. In this system, we uncover the physical principles of separation for simple nuclear arrays, and derive the microtubule-driven mechanical separation potential. We find that nuclei behave as cargo associated to self-organising microtubule asters which have repulsive properties. These results contrast with uninuclear model systems, where cortical pulling and hydrodynamic forces appear to drive aster movement and centring[19,29,30]. Our work reveals the underlying local biophysical interactions that pack and order nuclei within a rapidly changing active system.

Results

Synchronous nuclear duplication within a constant surface area poses a geometrical challenge (Fig. 1a, Supplementary Video 1). Spindle elongation during nuclear division[22] should cause transiently smaller distances between spindles (and their asters) unless some leave the surface after division. Alternatively, spindles may reorient their division axis to optimise the spacing between nuclei. We hypothesised that spatial patterns are related to mechanical interactions between spindle asters. Thus, we quantified neighbour distances (Fig. 1b), focusing on the distance d between centrosomes belonging to nearest neighbour nuclei ('non-sister'). Importantly, despite organelle duplication, synchronous spindle expansion (defined by s, Fig 1b), and apparent collective nuclear movement in a finite space, the distance distribution between neighbouring centrosomes within n.c. 10 did not exhibit noticeable decrease as a compensation (Fig. 1c, black dots, see also Methods). Similarly, or possibly as a result, the nuclear separation distance D only mildly decreased (Fig. 1d, black dots) during anaphase and telophase when nuclear duplication and mitotic separation occurs (Fig. 1d, blue dots). In subsequent division cycles, the mean distance between centrosomes gradually decreased while nuclear density doubled. Still, we observed no abrupt decrease or oscillation in the nuclear separation during duplication (Fig. 1e, Supplementary Fig. 1). These measurements suggest that a rigid mechanical connection exists between centrosomes. Thus, we hypothesised the presence of a repulsive mechanism between neighbouring nuclei or asters in the highly viscous, and effectively over-damped cytoplasm.

There appears to be no long-range order in spindle orientation across the embryo[12], but we asked whether there are local patterns. Defects may result in local ordering, akin to how subtle variations in sand corn size and shape induce fractures in sand piles with a range of lengths[31,32]. In the embryo, we investigated whether there were chains of aligned spindles (Fig. 1f and

Methods). Calculating the probability of a given chain length, L, in different cycles (Fig. 1g-h, Supplementary Fig. 2) we find $P(L) \sim L^{-\alpha}$, with $\alpha \approx 2.0 \pm 0.3$ in n.c. 13 (compared to $\alpha \approx 3.6 \pm 0.5$ with randomised spindle orientation). The value of α did not appear to decrease with increasing nuclear density (Fig. 1h), though it was dependent on the thresholds for defining chains (Methods). The value for α is similar to the exponent in cluster size variability in a range of other physical models[33–35]. Our results support the presence of short-range interactions driving spindle alignment.

We posited that repulsive interactions between astral microtubules underlie the forces determining the magnitude and spatial extent of the interactions determining spindle position and orientation. We consider a simple model of aster-aster interaction (Fig. 2a): (i) asters have a radial microtubule structure nucleated from a centrosome; (ii) asters are self-repulsive due to microtubule interactions, generating a "dumbbell"-like potential for each nucleus; and (iii) nearest neighbour interactions dominate over longer-ranged interactions. Each spindle has a single rotational degree of freedom (Fig. 2a, bottom). From our model (Methods), we predict (Fig. 2b): (i) two nearby isolated spindles will align in parallel and orthogonal to their connecting line (i.e., ϕ~90º); (ii) three equidistant spindles align at ϕ~60º to each other; (iii) four and more spindles align randomly. The system is geometrically frustrated for n>3 resulting in a broad range of possible states with the same energy minimum[36].

In embryos, with hundreds of spindles, these predictions for small systems cannot be tested experimentally. Thus, we took advantage of our embryo explant assay, which enables us to study a small number of spindles in quasi-2D spaces[26] (Fig. 2c-d, Supplementary Video 2). We measured spindle axis orientation ϕ relative to the separation axis (Fig. 1f). When a single spindle in an explant divides (Fig. 2d(i)), the two subsequent spindles align in parallel (Fig. 2d(ii)). Further divisions resulted in random spindle orientation, even when the spindles were uniformly distributed (Fig. 2d(iii), Supplementary Video 2). For three spindles, the alignment was biased away from random (p=0.04, Supplementary Fig. 3b-c), with some arrangements showing 60º alignment (Fig. 2d(iv), Supplementary Fig. 3a). However, we also observed cases where two out of three spindles aligned at 90º, likely due to the spindles not being positioned equidistant. The experimental observations were in agreement with our model predictions when stochasticity was introduced (Fig. 2e-f, Supplementary Fig. 3d-e and Methods). To conclude, the orientation and alignment of two-, three-, and four- syncytial mitotic spindles can be described by a model of mechanical dumbbells with nearest-neighbour repulsive interactions.

Centrosomes are essential for nuclear organisation in the embryo[23]. Are centrosomes, rather than nuclei, the active positioning structures in the early embryo? We propose that the aster repulsion is proportional to microtubule probability density and likely decays rapidly with distance δ from the MTOC (Fig. 2g). To test these ideas, we utilised *giant nuclei (gnu)* mutant embryos, which undergo DNA endoreplication without mitosis; chromosome segregation is inhibited, leading to one or few overgrowing (polyploid) nuclei, while centrosomes continue to duplicate and split[27,28,37] (Supplementary Video 3). We produced embryo explants from *gnu* mutant embryos and studied the positioning properties of a small number of microtubule asters in quasi-2D spaces. Asters consistently moved towards the centre of the explant, even when initially located near the boundary after cytosol deposition (Supplementary Video 4). We measured the shortest distance of the centrosome from the boundary at steady state, which varied between R/2 and the maximum distance R (Fig. 3a). Deviation from precise centring may be due to lipid droplets (green circles in Supplementary Video 4) forming exclusion zones. Typically, individual asters appear to self-centre within a restricted space, consistent with a radial force potential. Such short-ranged centring forces could be generated by microtubule polymerisation acting against the boundary of the water–oil interface[38,39]. Alternatively, hydrodynamic drag caused by microtubule motor transport together with radial asymmetry of asters can generate a net pulling force towards the centre[19]. In either scenario, once radial symmetry is restored the net force drops to zero.

How far do asters separate? We investigated the steady-state distribution of two-aster configurations in explants. Inter-aster interaction, if existing, must balance with the force involved in moving asters away from the boundary. Two asters reached a steady-state separation distance that scaled with explant size and boundary distances, typically up to 45 µm, but did not scale further in larger explants. Consequently, the shortest boundary distances were not always diametral (Fig. 3b, inset). For most explants the inter-aster distance and the shortest boundary distances were similar (Supplementary Fig. 4a-c). Interestingly, two asters did not separate according to equal force but approximately partitioned the available space ($d = b_1 = b_2 = 2R/3$). Some care is needed here though as (i) not all experiments covered the entire time course of aster separation; and (ii) some asters were likely initially positioned farther apart by the extraction procedure (red dots). Combined, these observations further support the presence of short-ranged repulsive interactions between asters and between aster and boundary. The two asters may mechanically interact via overlapping microtubules[40,41], while astral microtubules may simply hit against the boundary interface, which acts as an immovable hard wall.

162 In explants, as the number of asters further increases, the shortest distance between the aster and
163 boundary decreases (Fig. 3c-d). Interestingly, their steady-state position often assumed highly
164 ordered, almost crystalline configurations (Fig. 3c). Explants with higher numbers of asters had
165 reduced aster separation distances, likely due to increased internal compression of larger 2D aster
166 networks (Fig. 3e). Finally, in *gnu* mutant embryos, asters organise into a regularly spaced
167 network and reach a dynamic equilibrium once the cortex becomes fully occupied
168 (Supplementary Video 5). Quantifying inter-aster distance revealed a surprisingly stable and
169 reproducible pattern along time and between embryos (Fig. 3f, Supplementary Fig 4d-e).
170 Notably, the inter-aster distance d_a in *gnu* mutants at steady state and in multi-aster explants are
171 comparable, matching the non-sibling distance d observed in wildtype embryos (Fig. 1c),
172 strongly indicating that positional patterning of centrosomes in the syncytial embryo can happen
173 independently of embryo cortical factors, nuclei, spindle assembly and mitotic regulation.

174 Aster dynamics provide information about the underlying mechanical interactions. Single asters
175 located near the boundary after cytosol deposition stayed for up to 10 min, but they always
176 eventually migrated (Fig. 4a, Supplementary Fig. 5b & Video 4). Single asters moved rapidly
177 after separation from the boundary, with a maximum velocity of 0.05±0.02 μm/s, at around 20%
178 of its final distance from the explant boundary (Fig. 4b, Supplementary Fig. 5, Methods), before
179 linearly decelerating and stopping between 15–35 μm from the boundary (Supplementary Fig.
180 5b-d). There was only weak correlation between the final aster position and explant size, perhaps
181 due to steric effects from lipid droplets (Supplementary Fig. 5a-b). We noticed fewer
182 microtubules oriented outwards when the aster was near the boundary (Fig. 4c), suggesting a
183 lack of space for microtubule elongation. Indeed, in some samples we observed splay of
184 microtubules near the explant boundary (Supplementary Fig. 5e). Finally, we analysed the
185 dynamics of the lipid droplets that are also present in the explant, to infer about passive behaviour
186 from hydrodynamic effects. There was a droplet exclusion zone of ~10 μm around each aster.
187 As the aster moved away from the boundary, the lipid droplets streamed around the aster,
188 maintaining their exclusion (Supplementary Fig. 5f-g). We quantified the motion of lipid
189 droplets with and without an aster present (Supplementary Fig. 5h). In the absence of an aster,
190 the lipid droplets appeared to move randomly ($x_{rms} \sim t^{1/2}$). In the presence of an aster, lipid
191 droplets moved faster, and appeared to move in a more directed manner ($x_{rms} \sim t^{2/3}$). Such
192 behaviour is consistent with the aster having a repulsive force potential that can act on the
193 surrounding lipid droplets and other boundary constraints.

194 Next, we tracked aster pairs during separation (Fig. 4d-e, Supplementary Fig. 6 & Video 6). The
195 final distance between asters correlated well with explant size (Supplementary Fig. 6a).
196 Interestingly, the peak separation velocity was always near half the final aster separation distance
197 (Fig. 4e), independent of final separation distance. This contrasts with the single aster scenario
198 (Fig. 4b), suggesting that the overall effective forces are different in the two cases, consistent
199 with our observations in Fig. 3c-e. The aster separation could be driven by overlap and
200 crosslinking of microtubules[17], or by mutual contact leading to repulsion by microtubules of both
201 asters. We quantified the microtubule intensity between the separating asters (Fig. 4f, left) and
202 generated kymographs of the microtubule fluorescence intensity at half the separation distance
203 (Fig. 4f, right). The intensity exponentially decayed (Supplementary Fig. 6e), consistent with
204 models of dynamic microtubule length distribution[42,43]. When aster separation ceased there was
205 almost no measurable microtubule signal between the asters.

206 For a viscous material, the velocity, v, of an object is dependent on the applied force F: $v \approx \gamma F$,
207 where γ is the effective viscous drag coefficient. Naïvely interpreting the microtubule
208 distribution as the resulting force profile does not match with the observed separation velocity
209 profile. However, multiplying the microtubule distribution by an effective *slipping* term, $f_{slip} =$
210 $f_0 \frac{x^2}{x_0^2+x^2}$ ($x_0 \approx 15\ \mu m$), results in an excellent fit to our observed aster separation velocities (Fig.
211 4g). We attribute this effective slipping to molecular friction between microtubules[44]. Finally,
212 we noticed that the microtubule density between the asters was often not maximal along the
213 shortest distance between the asters (Supplementary Fig. 6f-g), suggesting that the contact
214 interfaces between asters is more complex than assumed above.

215 To explore the nature of the microtubule interaction, we performed a series of inhibitory
216 treatments. We generated explants with two asters in the course of separation and pulse-injected
217 a defined volume of 200 µM colchicine, which causes acute depolymerisation of microtubules.
218 Upon injection the asters stopped separating and sometimes inverted their direction of motion
219 (Fig. 4h, Supplementary Video 7). We then tested whether active molecular machinery was
220 required for aster repulsion by inhibiting ATP consumption. We injected a series of
221 concentrations of sodium azide into explants that contained a separating pair of asters
222 (Supplementary Video 7). Adding sodium azide decreased the initial recoil velocity (dashed lines
223 in Fig. 4h) and also resulted in a considerable reduction in aster separation. However, even at
224 very high concentrations of sodium azide, we still observed residual motion, suggesting that both
225 actively driven microtubule-mediated separation and passive physical contact driven separation
226 occur.

227 From our observations, we conclude that aster separation is caused by a net repulsive force
228 between asters and between aster and boundary. However, either pushing or pulling forces can
229 cause the separation dynamics and centring[29,45,46]. We performed targeted UV photo-ablation
230 experiments in explants and generated ellipse-shaped ablations positioned asymmetrically
231 around one aster, affecting microtubules on the left side more than on the right side of the aster
232 (Fig. 5a, Supplementary Video 8). If hydrodynamic effects from vesicle transport along
233 microtubules drives aster motion[19], we expect a displacement to the right (positive) after
234 ablation. Conversely, if the net force applied on microtubules favours pushing on MTOC, we
235 expect a displacement to the left (negative). Indeed, asters consistently moved to the left,
236 supporting a dominating effect of microtubule-driven pushing (Fig. 5b). As a control, we
237 performed the same perturbation in explants that were injected with the microtubule inhibitor
238 colchicine (Fig. 5c). Under this condition, asters moved very slowly to the right (positive), which
239 is consistent with a weak hydrodynamic effect from other contractile sources (*e.g.* actomyosin[47]).

240 To further test these conclusions, we performed two types of ablation in explants containing two
241 asters (Fig. 5d, Supplementary Video 9): (1) light pulses emitted along an ellipse around both
242 asters to destroy microtubules in the periphery; (2) light pulses emitted along a line between the
243 two asters to destroy microtubules between asters. If forces are attractive, then ablation type 1
244 will stop separation while ablation type 2 will lead to an acceleration. If forces are repulsive, we
245 predict the opposite response. We found a slight acceleration for peripheral ablation and a strong
246 deceleration with recovery for central ablation (Fig. 5e). Separation recovered likely because of
247 fast regrowth of microtubules after ablation (in the range of µm/min[48]). In summary, the dynamic
248 behaviour of asters in our explants is consistent with a model of radially symmetric microtubule
249 repulsion.

250 But, what is the relevance of our findings *in vivo*? Specifically, do the aster interactions enable
251 the embryo to pack the nuclei in a more regular manner? Heterogeneities in nuclear density are
252 a common phenomenon in early embryos resulting from aberrant cortical migration or nuclear
253 internalisation due to mitotic failure (Fig. 5f, Supplementary Fig. 7a). We predicted that nuclei
254 neighbouring a low-density region will orientate their division axis towards that region, where
255 repulsion is weakest. We identified such low-density regions and quantified the subsequent
256 division orientation of the surrounding nuclei (Methods), which confirmed our prediction (Fig.
257 5g, Supplementary Fig. 7b, Supplementary Video 10). Repeating the same analysis on regions
258 of uniform nuclear density showed no correlation in the division angle (Supplementary Fig. 7c).
259 We also generated acute density reductions by UV ablation. Using low laser damage, the target

nuclei failed to divide and detached from the cortex lowering local nuclear density (Supplementary Fig. 7d-e). Subsequently, the surrounding nuclei adjusted their division axis to orientate into the perturbed region (Supplementary Fig. 7f). Combining our results from spontaneous low-density regions and ablated embryos (including larger ablations of 3–5 nuclei), we see that the microtubule repulsion mechanism is efficient in adjusting the angle of division to compensate for heterogeneities in nuclear packing (Fig. 5h).

Discussion

Robust embryonic development critically depends on homogenous delivery of nuclei to the cell cortex and subsequent maintenance of a regular nuclear distribution despite further division cycles[15,16]. Recent work has shown how nuclear divisions are synchronised and, as a consequence, how nuclei are globally distributed around the embryo cortex[4,9]. However, these results assumed that nuclei are positioned regularly after each round of duplication[3]. Yet, what ensures such local order of nuclei? To answer this requires deepening our understanding of the biophysical principles defining the orientation of the spindle axis and how nuclei separate and reposition during division cycles. Our explant experiments demonstrate that, in the absence of perturbation by neighbour interactions, the ground-state orientation of a spindle is orthogonal to the previous division axis (Fig. 2f). This can be explained by the stereotypical migration of the two centrosomes from their common origin, each along one quadrant of the nucleus, until they form the poles of the bipolar spindle[49]. Hence, orthogonality of spindle axes likely emerges from the geometric nature of bipolar structures and symmetry considerations. Surprisingly though, a system of four or more spindles in a two-dimensional space evolves towards random orientations, arguing against active spindle orientation control by the cell. Our analysis suggests that force balancing and energetic minimisation in a noisy two-dimensional environment dynamically determine where nuclei are positioned and in which orientation they propagate upon division. Interestingly, in larger networks, small positional irregularities result in division axis orientation towards the low-density region, enabling the nuclear distribution to homogenise quickly and act as a self-repair mechanism. Finally, it would be interesting to compare aster force driving spindle alignment in the early embryo with similar microtubule-driven processes across cells, such as mitosis in polarised tissue growth[50].

Why is a high spatial regularity of nuclei important for the embryo? After n.c. 13, the embryo transforms into a multicellular embryo by engulfing each nucleus with plasma membrane[1]. The nearest neighbour internuclear distance defines cell size. Therefore, a narrow distance distribution leads to a uniform size of cells that subsequently assume distinct function during

body part definition. Analysis of information decoding in the *Drosophila* embryo has showed how each individual cell unambiguously reads its current position, which defines a specific function later in development[5]. But these results are dependent on the interpreting units (*i.e.* the nuclei) being uniformly distributed around the embryo. Therefore, we can conclude that a robust mechanism defining cell size and position is crucial as size irregularity would effectively decrease positional precision.

Acknowledgements

We thank members of the IAT and TES labs for fruitful discussions, and Virgile Viasnoff, Gianluca Grenci, Tetsuya Hiraiwa, Jacques Prost and Thomas Surrey for constructive comments and feedback. We thank the staff of the Fly Facility, the Advanced Imaging Facility (AIF) and the Technical Support Service at the Instituto Gulbenkian de Ciência (IGC). Transgenic fly stocks were obtained from Bloomington Drosophila Stock Center (NIH 741P40OD018537). We acknowledge financial support from: Human Frontiers Science Program (HFSP), awarded to IAT and TES and supporting JdC and ST (RGY0083/2016); Fundação Calouste Gulbenkian (FCG), the Fundação para Ciência e a Tecnologia (FCT) supporting IAT (Investigador FCT1072IF/00082/2013); EU FP7-PEOPLE-2013-CIG (Nº 818743) awarded to IAT and supporting JdC; LISBOA-01-0145-FEDER-007654 supporting IGC's core operation; LISBOA-01-7460145-FEDER-022170 (Congento) supporting the Fly Facility; PPBI-POCI-01-0145-FEDER-022122 supporting the AIF, all co-financed by FCT (Portugal) and Lisboa Regional Operational Program (Lisboa2020) under the PORTUGAL2020 Partnership Agreement (European Regional Development Fund).

Figures

(Figures 1–5)

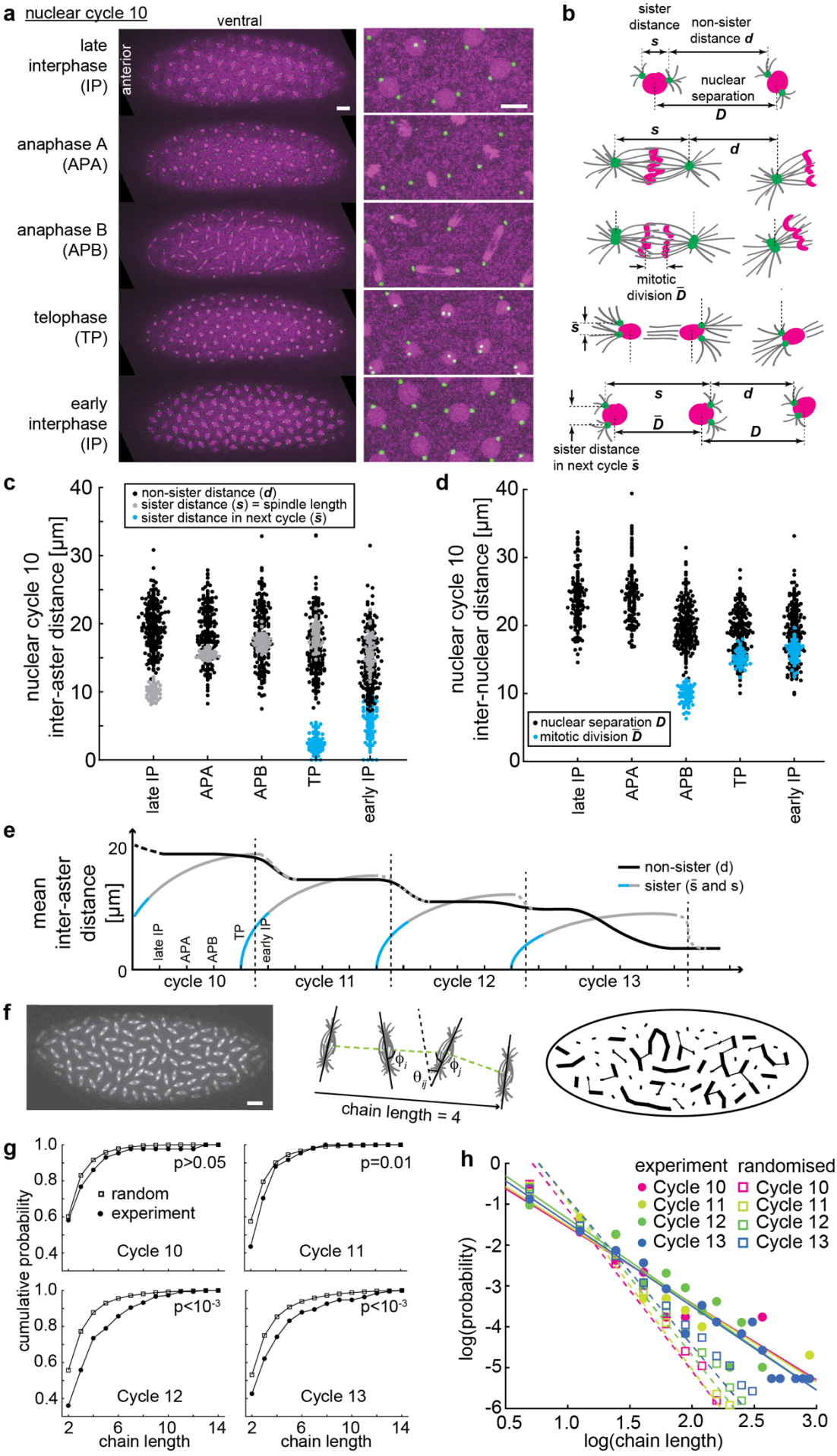
a
nuclear cycle 10
ventral
anterior
late interphase (IP)
anaphase A (APA)
anaphase B (APB)
telophase (TP)
early interphase (IP)
b
sister distance s
non-sister distance d
nuclear separation D
mitotic division D̄
sister distance in next cycle s̄
c
non-sister distance (d)
sister distance (s) = spindle length
sister distance in next cycle (s̄)
nuclear cycle 10 inter-aster distance [µm]
late IP
APA
APB
TP
early IP
d
nuclear cycle 10 inter-nuclear distance [µm]
nuclear separation D
mitotic division D̄
e
mean inter-aster distance [µm]
non-sister (d)
sister (s̄ and s)
cycle 10
cycle 11
cycle 12
cycle 13
f
chain length = 4
g
cumulative probability
p>0.05
p=0.01
p<10-3
random
experiment
Cycle 10
Cycle 11
Cycle 12
Cycle 13
chain length
h
experiment
randomised
log(probability)
log(chain length)

Fig. 1 – Spindle separation and orientation in the syncytial blastoderm of *Drosophila melanogaster* reveals robust distance maintenance and local orientation patterns. (a) Time lapse (maximum intensity Z-projections) (Supplementary Video 1) from an embryo expressing H2Av::RFP (magenta) and Spd2::GFP (green) during n.c. 10 (scale bar, 20 µm left, 10 µm right). Each panel corresponds to the indicated mitotic phase. **(b)** Morphological identification of mitotic phases and hierarchical classification of distances; extended figure legend in Supplementary Fig. 1. **(c-d)** Inter-aster (**c**) and nuclear (**d**) distance during n.c. 10 (n=15 spindles, N=5 embryos). **(e)** Schematic of average inter-aster distances during blastoderm n.c. 10–13 (also Supplementary Fig. 1). **(f)** Maximum intensity Z-projection of an embryo in n.c. 11, expressing Jupiter::mCherry (scale bar, 20 µm). Schematic illustrates how neighbouring spindles belonging to an alignment ('force') chain form angles θ and ϕ relative to each other (details in Supplementary Fig. 2a-b). Resulting chains are shown on the right; lines denote connections that satisfy two (thick) or only one (thin) of the conditions defining a chain (Methods). **(g)** Cumulative probability function of chain length for different cycles (n=7 embryos each for n.c. 10, 11, 12, 13). P-value calculated from Kolmogorov-Smirnov test. **(h)** Scaling of chain length probability with chain length for n.c. 10–13. Lines represent fit to $\beta L^{-\alpha}$, where L is the chain length and α is the scaling exponent (Methods).

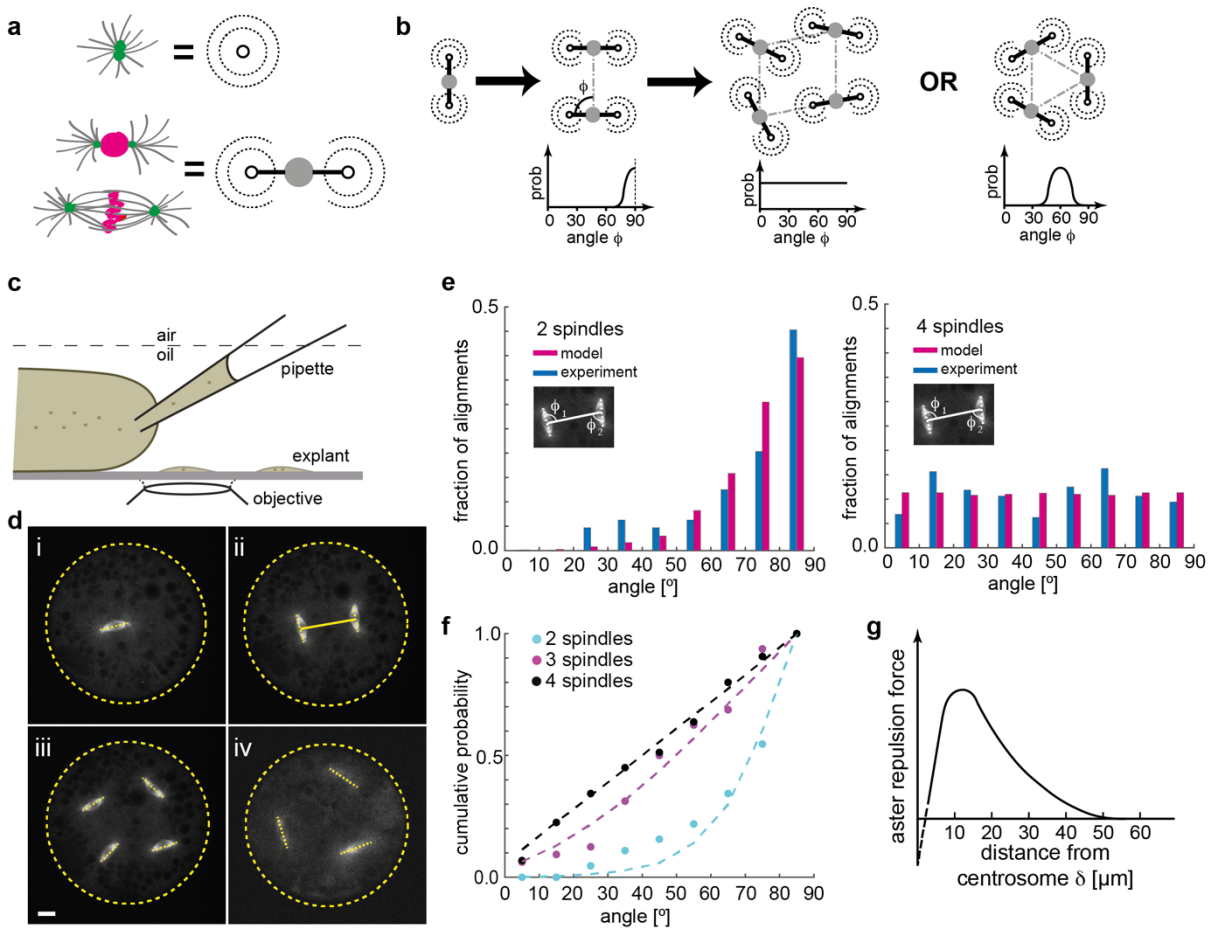

Figure 2 – Division axis orientation for 2–4 spindles in a cytosolic explant are consistent with a simple dumbbell model of aster repulsion. (a) Schematic of an aster, polymerised and organised by a centrosome (green), which translates into a concentric repulsion potential, here represented by dashed circles. When two asters are coupled to a nucleus (magenta) the repulsive potentials translate into a dumbbell potential with a rotational degree of freedom. **(b)** Scheme of dumbbells representing spindles in consecutive divisions. The graphs below show the expected probability of division angles ϕ between dumbbell axes from free energy considerations (Methods). Right panel shows predicted alignment for a three-spindle arrangement. **(c)** Schematic of cytosol extraction from a *Drosophila* syncytial embryo and explant formation. **(d)** Maximum intensity Z-projections of explants from embryos expressing Jupiter::GFP (grey) and H2Av::RFP (not shown) containing different numbers of spindles (10 μm scale bar). **(e)** Angle between the division axes of two spindles (left, n=32 explants) and between nearest neighbour spindles in a four-spindle scenario (right, n=40 explants) as measured in experiments (blue) or obtained from simulation (magenta, Methods). **(f)** Cumulative probability of the angle between division axes for two-, three- (n=5 explants) and four-spindle scenarios. Dashed lines are model predictions. **(g)** Proposed repulsion force as function of distance from the centrosome (green in

a) with peak at ~15 μm and negligible for >45 μm. The dashed line represents the short-distance interaction regime that is below the diffraction limit of optical resolution.

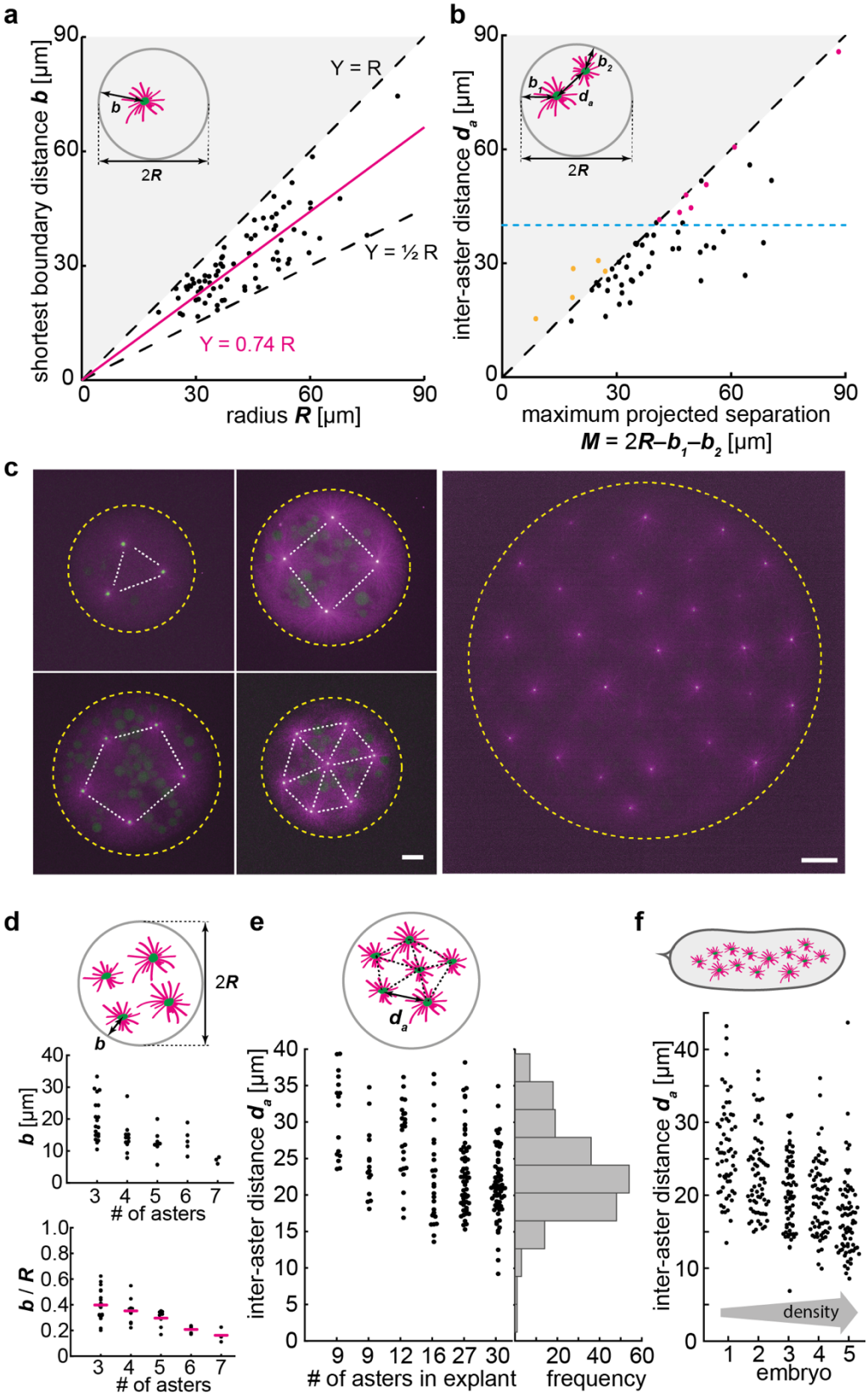

355

356 **Figure 3 – Free asters separate and achieve steady-state distance regularity. (a)** Explant
357 with single aster: scatter plot of the shortest distance to the boundary (b, see inset) as a function
358 of the explant radius (R) (n=78). Magenta line: linear regression with zero intercept. **(b)** Explant
359 with two asters: scatter plot of inter-aster distance (d_a, see inset) as a function of the maximum

projected separation M, calculated from the explant diameter (2R) and the boundary distance of each of the two asters (n=54). The blue dashed line represents the estimated upper limit of the interaction distance between two asters (~45 µm). Red dots represent cases where the two asters were likely positioned far apart during explant generation. The yellow dots are cases of small explants where projection leads to overestimation of b (Methods) **(c)** Maximum intensity Z-projections of explants containing multiple asters extracted from *gnu* mutant embryos expressing RFP::β-Tubulin (magenta) and Spd2::GFP (green) (scale bar, 10 µm). Dashed yellow circle represents the explant boundary, and white dashed lines highlight the symmetry in the aster distribution. **(d)** Distribution plot of shortest boundary distance (b, top scheme) and the ratio b/R from explants containing 3 (n=19), 4 (n=11), 5 (n=8), 6 (n=5) and 7 (n=3) asters. Magenta bars represent mean value. **(e)** Distribution plot of inter-aster distance (d_a, see inset) of single explants containing nine or more asters. **f)** Scatter plots of inter-aster distance from five *gnu* mutant embryos in order of increasing aster density.

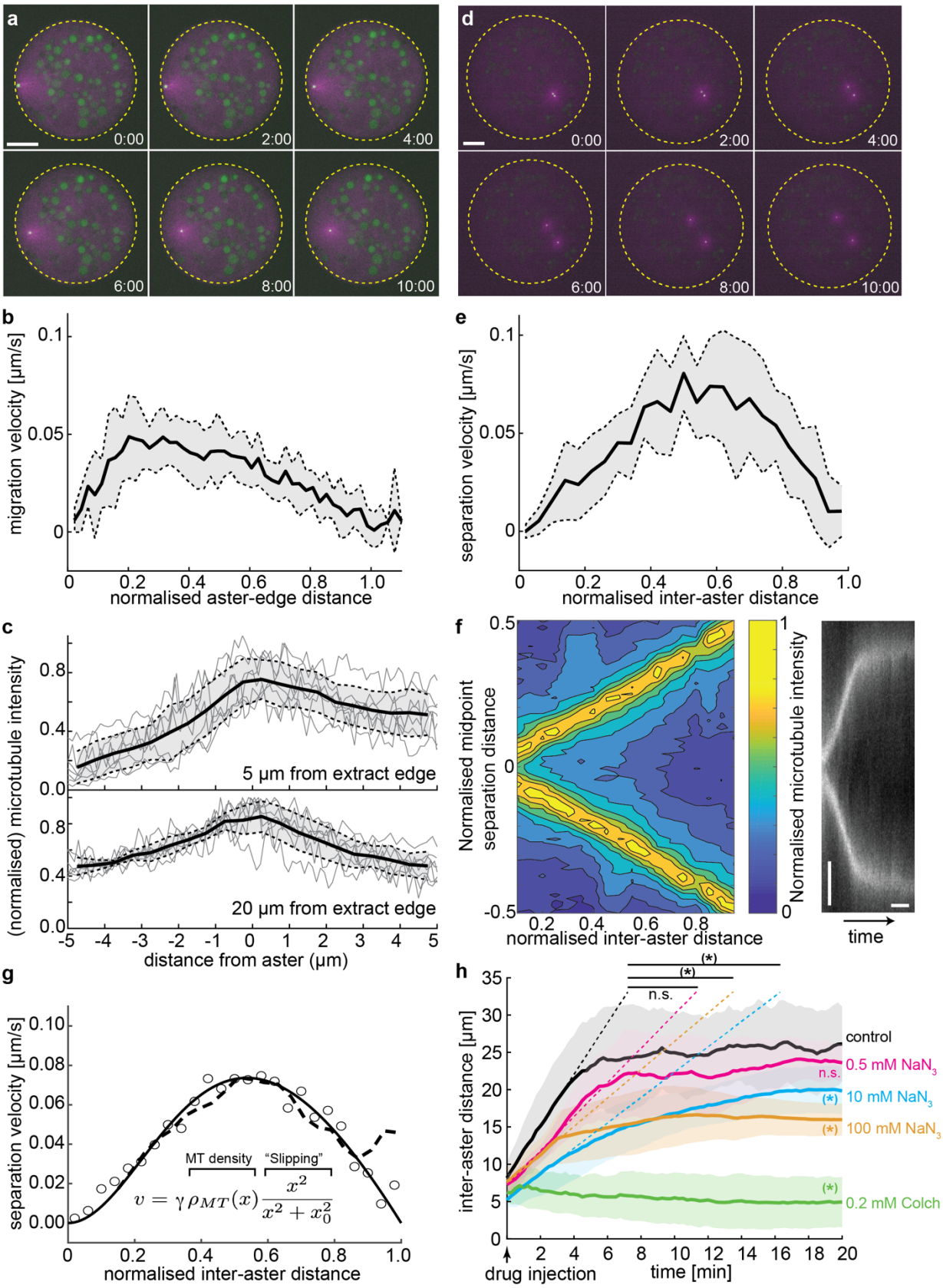

Figure 4 – Aster dynamics in explants depends on microtubule distribution and interactions. (a) Maximum intensity Z-projections of a single aster moving away from the boundary of an explant produced from *gnu* mutant embryos expressing RFP::β-Tubulin

377 (magenta) and Spd2::GFP (green). Scale bar, 20 µm **(b)** Average migration velocity of single
378 asters away from the explant boundary (n=7). Distance normalised by the final, steady-state
379 distance for each aster (also Supplementary Fig. 5a). **(c)** Average microtubule density (black
380 line, inferred from RFP::β-Tubulin signal) along shortest distance to explant boundary,
381 normalised by the maximum intensity within each experiment. Grey traces are individual
382 experiments (n=7). **(d)** As in (**a**) but for an explant containing two separating asters. **(e)** Aster
383 separation velocity as a function of normalised separation distance (n=9). For each experiment,
384 distance is normalised by the final, steady-state separation distance (also Supplementary Fig. 6).
385 **(f)** (left) Colourmap of normalised microtubule density (as in **c**) between two separating asters.
386 (right) Kymograph of microtubule intensity between the asters during separation. Scale bars, 2
387 min (horizontal) 5 µm (vertical). **(g)** Fitting to average separation velocity (circles) considering
388 microtubule intensity and a microtubule slipping term. Microtubule density was either fitted
389 beforehand (solid line, Supplementary Fig. 6e) or directly included (dashed line). **(h)** Aster
390 separation dynamics upon injection of buffer (control, n=3), 0.5 mM (n=3), 10 mM (n=4),
391 100mM (n=3) sodium azide, or 0.2 mM (n=3) colchicine. * denotes $p<0.05$. Grey or coloured
392 areas around average curves in **b**, **c**, **e** and **h** denote ± 1 s.d.

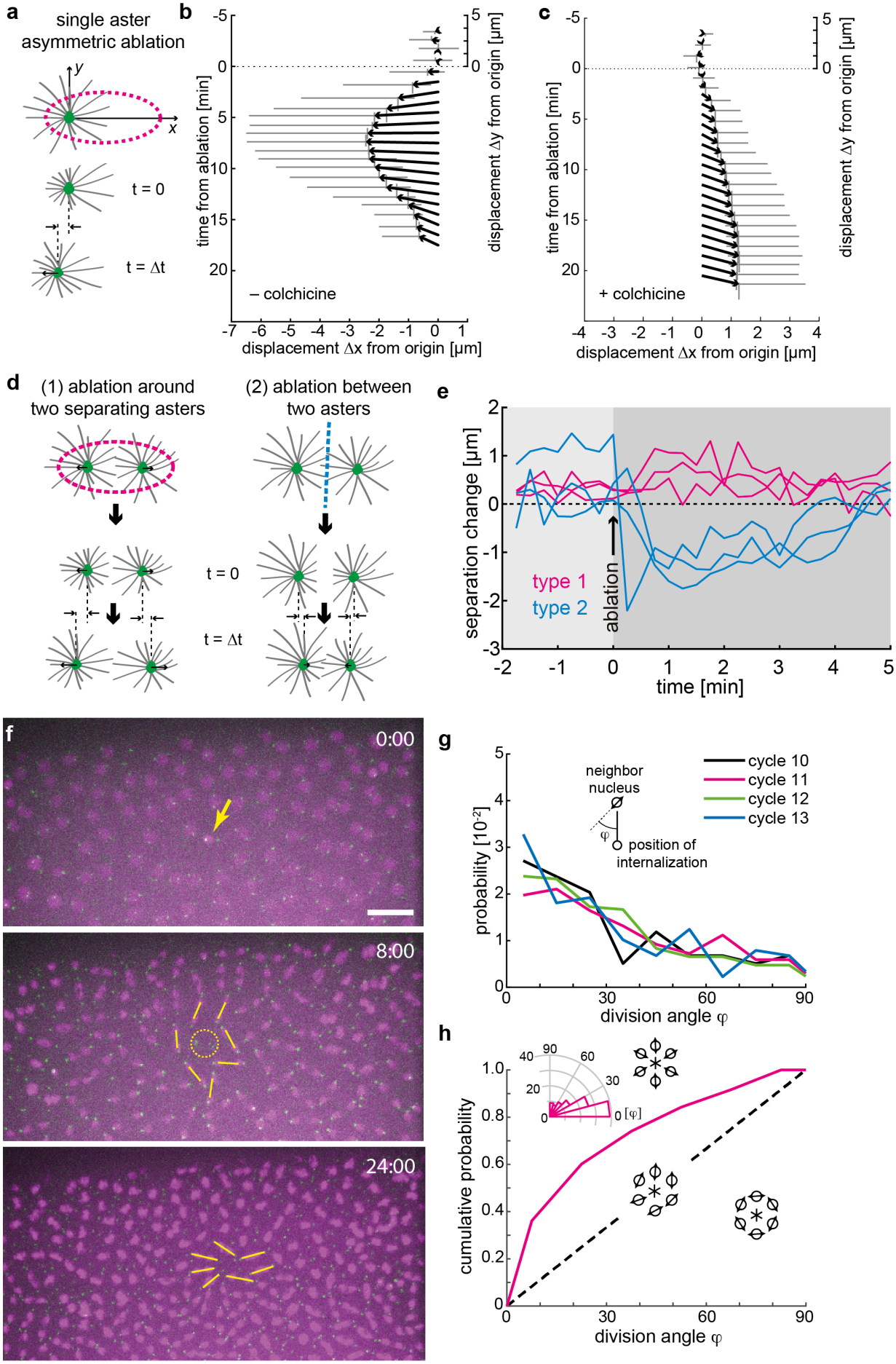
a
single aster
asymmetric ablation
y
x
t = 0
t = Δt
b
time from ablation [min]
displacement Δy from origin [μm]
– colchicine
displacement Δx from origin [μm]
c
time from ablation [min]
displacement Δy from origin [μm]
+ colchicine
displacement Δx from origin [μm]
d
(1) ablation around
two separating asters
(2) ablation between
two asters
t = 0
t = Δt
e
separation change [μm]
type 1
type 2
ablation
time [min]
f
0:00
8:00
24:00
g
probability [10-2]
neighbor
nucleus
position of
internalization
cycle 10
cycle 11
cycle 12
cycle 13
division angle φ
h
cumulative probability
division angle φ

393

Figure 5 – Microtubule-dependent repulsion provides a mechanism for spindle alignment towards lower density. (a) Schematic of single aster eccentric circular UV laser ablation (magenta dashed line); t=0 min denotes ablation time. **(b,c)** Aster displacement before and after ablation in explants unperturbed (**b**) or treated (**c**) with colchicine. Arrows represent average displacement magnitude and direction, and vertical and horizontal grey bars denote ± 1 s.d. of displacement in x and y, respectively. **(d)** Two-aster ablation procedure: (1) ellipse ablation around two asters during separation; (2) linear ablation between two asters. **(e)** Change of inter-aster distance upon laser ablation (at t = 0 min) as described in (**d**). **(f)** Maximum intensity Z-projections from an embryo expressing H2Av::mCherry (magenta) and Spd2::GFP (green) in n.c. 12–13. Yellow arrow (top panel) denotes internalisation of a nucleus. The centrosomes remain at the embryo cortex (yellow circle, middle panel). Division axes of neighbouring spindles (yellow lines) orientate towards the location of internalisation in n.c. 13 (bottom panel). Scale bar, 20 µm; time in min:sec. **(g)** Probability density function of the division angle orientation φ of neighbouring nuclei to regions of low nuclear density in n.c. 10–13 (n=67, 116, 96, 73 angles from N=10, 15, 15, 15 embryos in n.c. 10, 11, 12, 13 respectively). **(h)** Cumulative distribution function of division axis angle at the end of n.c. 13 towards artificially generated holes generated by single-pulse UV laser ablation (n=108 angles from 15 embryos). The dashed black line represents random division orientation (also Supplementary Fig. 7).

Materials and Methods

Fly strains

Flies with genotypes w^{1118}; +; endo>Jupiter::GFP (stock no. 6836, Bloomington) and w*; +; endo>H2Av::RFP (stock no. 23650; Bloomington) were crossed to generate recombinant progeny. Similarly, flies expressing fluorescent reporters recombined on the 2nd chromosome were produced by crossing the following stocks: w*; endo>H2Av::RFP; + (stock no. 23651; Bloomington); w*; pUbq> β-Tubulin::EGFP; + (stock no. 109603, Kyoto) ; w*; pUbq>RFP::β2-Tubulin; + (see Reference[51]) and w^{1118}; pUbq>Spd2::GFP; + (all provided by Mónica Bettencourt Dias, Instituto Gulbenkian de Ciência, Portugal). All resulting recombinant fly lines are homozygous viable. w^{1118}; +; Jupiter::mCherry flies were generated by and obtained from Nick Lowe in Daniel St Johnston's lab (The Gurdon Institute, United Kingdom). H2Av::mCherry flies were generated as described elsewhere[13]. Two different mutants of giant nucleus (*gnu*), namely w*; +; gnu^{305}/TM3 (discontinued stock no. 3321; Bloomington) and w*; +; $gnu^{Z3-3770A}$/TM3 (discontinued stock no. 38440; Bloomington), were each balanced with w^{1118}; CyO/Sco; MKRS/TM6B (stock no. 3703, Bloomington). Above described recombined

427 lines on the 2nd chromosome were individually crossed with gnu mutants and kept as balanced
428 stocks. Finally, trans-heterozygous were generated for $gnu^{305}/gnu^{Z3-3770A}$ mutants, whereby only
429 flies homozygous for the fluorescent reporters on the 2nd chromosome were selected for
430 increased signal collection during live microscopy. These trans-heterozygotes laid fertilized eggs
431 which undergo several embryonic rounds of chromatin replication and centrosome duplication,
432 allowing for the study and quantification of asters at the embryo cortex.

433 ***Embryo collection and sample preparation***

434 We followed established procedures[52] of fly husbandry, keeping flies at 25°C under 50-60%
435 humidity. For embryo collections, young adult flies were transferred to a cage coupled to an
436 apple juice agar plate. After 2–3 rounds of egg laying synchronisation, developing embryos were
437 collected every 30–60 minutes. In the case of *gnu* mutants, embryos were collected at different
438 time intervals, ranging from 30 min up to 4h. Embryos were dechorionated by short immersion
439 in 7% sodium hypochlorite solution (VWR). After extensive rinsing with water, embryos were
440 aligned and immobilised in a thin strip of heptane glue placed on 22x22mm coverslips, and
441 covered with halocarbon oil (Voltalef 10S, Arkema).

442 ***Microscopy***

443 Time-lapse acquisitions were conducted on a Nikon Eclipse Ti-E microscope equipped with a
444 Yokogawa CSU-W Spinning Disk confocal scanner and a piezoelectric stage (737.2SL, Physik
445 Instrumente). For embryo imaging, 15 µm (31 planes) Z-series stacks were acquired every 15s,
446 using a Plan Fluor 40x 1.3NA oil immersion objective, the 488nm and 561nm laser lines, and an
447 Andor Zyla 4.2 sCMOS camera to acquire images. For explants up to 100µm in diameter, we
448 used a Plan Apo VC 60x 1.2NA water immersion objective with 2x post-magnification and an
449 Andor iXon3 888 EMCCD camera. When needed, the Andor Zyla 4.2 sCMOS camera was
450 selected to acquire a 2x wider field of view with the same spatial resolution or, alternatively, the
451 Apo λ S LWD 40x 1.15NA water immersion objective.

452 ***Single embryo explant assay***

453 Embryo extractions were performed as previously described[26,53]. Briefly, cytosol from wild-type
454 embryos between telophase and subsequent interphase of cycle 8 was extracted by puncturing
455 the vitelline membrane with a sharp glass micropipette and flow control by operating a bi-
456 directional syringe pump. Small explants of cytosol (in the picolitre range) were deposited on
457 poly-L-lysine coated glass surface under halocarbon oil. Time-lapse acquisitions typically
458 started in late interphase or prophase. In the case of *gnu* mutant embryos, most extractions were
459 performed when few centrosomes (between 5 and 40) were visible at the anterior-lateral cortex.

460 During extractions, shear stress was avoided to prevent structural damages and undesirable
461 molecular dissociations that induce premature mitotic failures or aberrant microtubule structures.
462 In *gnu* mutant embryos, repeated use of the same extraction micropipette is not recommended.
463 Explants from wildtype embryos initially containing a single nucleus were selected for time-
464 lapse imaging of subsequent mitotic divisions. Explants from *gnu* mutants initially containing a
465 single free aster near oil interface or two free asters in close proximity were selected for time-
466 lapse imaging of aster separation. All experiments were conducted at 25±1 °C.

467 ***Pharmacological perturbation of embryo explants***

468 Pharmacological perturbations were performed by adding different drugs (colchicine at 0.2 mM,
469 sodium azide at 0.5, 10, or 100 mM) diluted in cytoplasm-compatible buffer (50 mM HEPES,
470 pH 7.8, 100 mM KCl, 1 mM $MgCl_2$). Solutions were directly administrated to the explants using
471 a fine pipette (pulled using a Narishige PC-100 Puller with a: 2-step (69% + 55%) heating
472 protocol and with 4 mm drop length) connected to an Eppendorf FemtoJet® 4i pump. The final
473 drug dilution in the explants was of approximately 1:10 (solution:cytosol). Buffer injections were
474 conducted as control.

475 ***Laser ablation system***

476 The laser ablation systems used for experiments with intact embryos (at EMBL Heidelberg,
477 described elsewhere[22]) and embryo extracts (at Instituto Gulbenkian de Ciência, implemented
478 by IA Telley on the microscope described above) were conceptually identical. A Crylas FTSS-
479 355-Q pulsed laser emitting 355 nm, 1.1 ns pulses, 15µJ pulse energy at 1 KHz was aligned with
480 a beam expander (16x), a scan head (SCANcube 7, Scanlab, Germany) coupled to an f-theta lens
481 (f=56 mm, anti-reflection coating for 340–370 nm, SCANLAB AG, Germany). The focus point
482 of the f-theta lens was aligned to be parfocal to the focal plane of the objective, using a tube lens
483 (f=200 mm, Ø=30 mm, 355 nm AR coated, OWIS, Germany) and a dichroic mirror (T387
484 DCLP, Chroma) in the upper stage filter wheel. Any scattered light was blocked at the emission
485 side with a RazorEdge LP 355 dichroic mirror OD6 @ 355nm (Chroma). The system was
486 controlled with homemade journals for Metamorph software (Molecular Devices Inc.). The
487 optimal laser power was set to ensure microtubule ablation while avoiding thermal expansion of
488 cytoplasm, with post-ablation microtubule signal recovery matching known polymerisation
489 dynamics. This combination of conditions proved to be efficient at ablating target structures
490 beyond fluorophore bleaching. In explants containing a single aster, astral microtubules were
491 asymmetrically ablated by positioning an ellipsoid off-centre (21.7 by 10.8 µm, 4 times, 15s
492 interval, 0.54 µm step, laser power: 25%) (Fig. 5a). In explants containing two asters, astral

microtubules were ablated using an ellipsoid (21.7 by 10.8 µm, 3 times, 15s interval, 0.54 µm step, laser power: 10–15%) roughly centred at the mid-point between the two asters, while interpolar microtubules were ablated using linear ablations (21.7 µm, 3 times, 15s interval 0.54 µm step, laser power: 10–15%) perpendicular to the axis connecting the asters (Fig. 5d).

Distance analysis in embryos

Automated positional detection of the signals from centrosomes and nuclei (or chromatin) was performed by applying a Gaussian blur filter (radius: 1–2 pixels) and using the plugin TrackMate v3.5.1 in FIJI ImageJ[54,55]. The coordinates of detected spots were imported into MATLAB® for assignment and distance calculation. The connection between poles belonging to a spindle structure was assigned in a custom-made script requiring user input, on an area containing 15–40 spindles for each mitotic phase and per embryo. For each spindle–assigned coordinate positions, the nearest neighbour positions were determined using the Delaunay triangulation functions in Matlab® yielding a connectivity list. Thereby, a spindle structure is defined as a combination of n centrosome and m chromatin positions (n,m) with the following numbers for mitotic phases: late interphase (2,1); anaphase A (2,1); anaphase B (2,2); telophase (4,2), early interphase (4,2). With this assignment, the duplicated organelles dissociate at the transition from telophase to early interphase, so that two related nuclei become independent neighbours. Next, the 3D Euclidean distances between relevant positions were calculated from position coordinates with a computer-assisted manual heritage classification. The distance between separating chromosomes $\overline{D}$ was calculated from the two chromatin entities within a spindle. Spindle length s was calculated from the distance between two centrosomes belonging to each spindle. In phases with four centrosomes per spindle, two at each pole, spindle length was defined as the smallest distance between opposite centrosomes (four possible combinations). The sister centrosome distance $\bar{s}$ was calculated from centrosome pairs at each spindle pole. Inter-aster distance d (corresponding to the distance between non-sister centrosomes) was calculated between different, neighbouring spindles by selecting all centrosomes not associated with the same spindle from the nearest neighbour connectivity list. Inter-nuclear distance D was calculated between nearest neighbour nuclei or chromosomes not belonging to the same spindle. Finally, the arithmetic mean and standard deviation of the distance distributions within a single embryo were calculated and overlaid for division cycles 10–13 (Supplementary Fig. 1). In *gnu* mutant embryos, inter-aster distance d_a was calculated from a selected region containing 15–20 centrosomes, for each embryo at different time points using triangulation and neighbourhood connectivity list. Centrosomes located at the anterior hemisphere were excluded to avoid the influence of the giant polyploid nucleus. The *gnu* mutants present variable centrosome densities

depending on age and other unknown factors. We analysed the variation of distance distribution for five different embryos with similar densities during intervals of 10 min. All data plots were generated in MATLAB®.

Spindle alignment analysis in embryos

For each embryo, we took the time point two minutes prior to the first onset of nuclear division. The angle of the centrosome pair was used to define an orientation angle for the spindle.

In calculating the force chains, we did the following for each cycle:

1. For each spindle *i*, identify nearby spindles (taken as 1.3 times {average nearest neighbour distance});

2. Calculate the orientation angle difference between pairs of nearest spindles. This value can range between 0º and 90º (as there is no direction to the spindle orientation). We define this angle as θ_{ij} for each pair of spindles denoted by *i* and *j* respectively.

3. Find the vector between each spindle and its nearest neighbours $\mathbf{x}_{ij}$. Find the angle, ϕ, between the orientation of the spindles *i* and *j* relative to $\mathbf{x}_{ij}$. As the orientation does not have a specific direction, for angles >90º we define Φ = 180 – ϕ.

4. We tested different thresholds on θ and ϕ (annotated by $\Delta\theta$ and $\Delta\phi$) to find the chain length frequency (Supplementary Fig. 2c). For a spindle to belong to a chain, at least the angle θ had to meet the condition $0 \leq \theta \leq \Delta\theta$. In addition, a second condition was defined: $\Delta\phi \leq \phi \leq 90°$. Neighbouring spindles that meet both conditions belong to a chain that exhibits alignment both along the chain axis and between spindles. In the below table, we give the fitted value of α (as defined in main text) for different constraints on θ and ϕ.

Cycle	$\theta = \phi = 45º$	$\theta = 45º, \phi = 30º$	$\theta = 30º, \phi = 45º$	$\theta = \phi = 30º$
10	1.9	2.7	2.7	3.4
11	1.9	3.3	2.9	4.0
12	2.1	3.1	3.4	3.8
13	2.0	3.4	3.0	4.6

Table 1A: α for different conditions on chain alignments for experimental data

Cycle	$\theta = \phi = 45º$	$\theta = 45º, \phi = 30º$	$\theta = 30º, \phi = 45º$	$\theta = \phi = 30º$
10	4.0	5.1	4.7	4.6
11	4.1	5.0	4.8	6.0
12	3.8	4.7	4.7	5.5
13	3.6	4.8	4.4	5.6

Table 1B: α for different conditions on chain alignments for randomised data

551 ***Spindle alignment in explants***

552 Extracts initially containing 2, 3 and 4 dividing nuclei were analysed in terms of spindle axis
553 orientation by analysis of microtubule reporters at the onset of anaphase B. Using MATLAB®
554 home-made scripts, the two minor orthogonal angles (ϕ_1 and ϕ_2) were determined by manual
555 clicking at spindle poles. These angles can range between 0º (parallel orientation) and 90º
556 (perpendicular orientated).

557 ***Dumbbell model of nuclear alignment in explants***

558 For the model, we consider a simple phenomenological model: $H = J\sum_{<i,j>}(\overrightarrow{S_i}.\vec{r}_{i,j})^2$, where $\vec{S}_i$
559 represents the orientation of aster *i* (with $|S_i| = 1$) and $\vec{r}_{i,j}$ is the unit vector between aster *i* and
560 its nearest neighbours *j*. The model is quadratic as there is no preferential direction for *S*. In this
561 case, energy is minimised if nuclei align perpendicular to the vector of separation, $\vec{r}_{ij}$, between
562 nuclei. In the case of two nuclear spindles, it is clear this results in parallel aligned nuclear
563 spindles, both of which are perpendicular to the vector between the nuclei. For three spindles,
564 positioned at (0,0), (1,0) and $(\frac{1}{2},\frac{\sqrt{3}}{2})$, the energy is minimised for $S_1 = \left(-\frac{1}{2},\frac{\sqrt{3}}{2}\right), S_2 = (\frac{1}{2},\frac{\sqrt{3}}{2})$
565 and $S_3 = (1,0)$ (direction of the vectors can also be inverted). We use a Metropolis algorithm to
566 simulate the alignment of asters at different effective temperatures *T*. There is only one
567 parameter, defined by J/k_BT, which represents the competition between alignment force (*J*) and
568 random fluctuations (k_BT). In Supplementary Fig. 3d-e, we show simulation outputs for $\frac{J}{k_BT} =$
569 10^{-3} and 10^0 . Result presented in Fig. 2 are for $\frac{J}{k_BT} = 10^{-1}$.

570 Of course, we can consider more complex models, such as $H = J\sum_{<i,j>}\big(1 -$
571 $(\overrightarrow{S_i}.\vec{S}_j)^2\big)(\vec{S}_i.\vec{r}_{i,j})^2$ which incorporate both terms involving neighbouring aster alignment and
572 their alignment relative to $\vec{r}_{ij}$. There is also similarity to models of nematic ordering in liquid
573 crystals[33], which have recently been applied to other biological systems[56]. Studies of self-
574 propelled particles with repulsive interactions are also relevant, where longer ranged interactions
575 are also considered[57]. Our aim here is to simply show how simple dumbbell-like repulsion
576 (which results in one rotational degree of freedom) can lead to different behaviours depending
577 on the system topology, not to build a precise model for how such potentials interact.

578 ***Analysis of free asters in explants – distance distributions***

579 Distance between asters and from aster to the boundary were obtained in explants at steady state,
580 *i.e.* where asters did not move anymore (usually 30–45 min after explant deposition). The inter-
581 aster distance was determined as Euclidean distance in 3D. We defined the *boundary distance*

582 (b, b_1, b_2) as the shortest distance from the aster to the interface between glass, oil and cytosol,
583 determined manually using the FIJI measurement tools (at a precision of ±0.5 µm). To determine
584 the explant boundary on the glass (approximated with a circle of radius R), maximum intensity
585 projections of both fluorescence emission channels was assessed to trace the interface between
586 the glass, oil and cytosol. For larger explants with high aspect ratio – a quasi-2D situation – the
587 definition of *boundary distance* served as good approximation for a boundary in two dimensions.
588 However, in small explants where the aspect ratio is not as high, two asters sometimes aligned
589 considerably in the third dimension. In these cases, the definition for *boundary distance* led to
590 an underestimation of the maximum projected inter-aster distance $M = 2R - b_1 - b_2$; it
591 becomes a geometric problem in 3D and the longest dimension is not necessarily in the plane of
592 the glass-explant interface. This is evident for some data points in small explants (yellow dots in
593 Fig. 3b).

594 ***Analysis of free asters in explants – dynamics***

595 The coordinates of free asters were obtained by applying a Gaussian blur filter (radius: 1–2
596 pixels) and using the plugin TrackMate v3.5.1 of FIJI ImageJ[54,55]. The coordinates of detected
597 spots were imported into MATLAB® for assignment and distance calculation similarly as
598 mentioned above.

599 The instant relative velocity was calculated using the formula: $v_i = \frac{d_{i+1} - d_{i-1}}{t_{i+1} - t_{i-1}}$, where d is the 3D
600 Euclidian distance and t is time in the flanking time points of the measure point.

601 For unperturbed experiments, data was normalised to the maximum distance achieved in the
602 separated phase in order to correct for scaling effect during splitting dynamics (Fig. 4). This data
603 was fitted to the phenomenological equation (Supplementary Fig. 6b):

604 $$u = a + b \cdot \tanh\left(\frac{t}{\tau}\right)$$

605 To analyse the lipid droplets, we performed a similar analysis using FIJI TrackMate. Seven
606 extracts were analysed with an aster present, with over 100 individual tracks of lipid droplets.
607 RMS distance was then extracted across the entire time course of imaging. Similar analysis was
608 performed in extracts without an aster. Curves (Supplementary Fig. 5h) were fitted using the 'fit'
609 function in MATLAB®, with $r^2 = 0.98$ ($b \cdot t^{\frac{1}{2}}$ for no-aster data), $r^2 = 0.96$ ($a_1 \cdot t^{\frac{1}{2}}$ for 1-aster data),
610 and $r^2 = 0.99$ ($a_2 \cdot t^{\frac{2}{3}}$ for 1-aster data). Fitting the general function $a \cdot t^c$ gives a best fit for $c =$
611 0.66 for the one aster data.

612 ***Microtubule profile quantification***

613 For single asters (Fig. 4a-c), we quantified the microtubule intensity using the intensity of the
614 RFP::β-Tubulin signal. Taking the point when asters were either 5 μm or 20 μm from the explant
615 boundary, we used FIJI to measure the microtubule intensity along a 10 μm straight line from the
616 edge and through the aster. The line had a width of 2 μm. For each experiment, we normalised
617 the total intensity by the maximum measured value and then binned the data in 0.2 μm bins.
618 Hence, the recorded intensity does not reach one, and the mean intensity only reaches a
619 maximum around 0.8 as the maximum value does not occur at the same position.
620 Similar analysis was performed for the scenario with two asters (Fig. 4d-g). In this case, the
621 centroids of the asters were used to define a straight line along which the microtubule intensity
622 was measured throughout the process of aster separation. From this straight line between the
623 asters, we also generated the kymograph shown in Fig. 4f right.

624 ***Analysis of free asters in explants – perturbations with drugs and UV ablation***
625 For comparison between control and perturbation experiments, data was time-aligned to the
626 perturbation time-point (t=0) and plotted as average ± s.d. from at least three replicates for each
627 condition. The change of inter-aster distance during the first 3 s after drug injection was
628 estimated by linear regression, and the confidence interval of the slope served as significance
629 test. Differences in steady-state inter-aster distance were tested by comparing the pools of
630 distances from the last 3 s, using Wilcoxon signed-rank test. A significance level of 0.05 was
631 defined prior to testing. In the case of UV ablations, the position of the aster five frames before
632 ablation was defined as coordinate origin. The two main axes of the ellipsoid, along which the
633 pulsed ablation was performed, defined the cartesian coordinate system. A displacement vector
634 of the current aster position relative to the origin was calculated for each time point. The mean
635 and standard deviation of axial (Δx) and lateral (Δy) displacement was plotted in time (Fig. 5b-
636 c).

637 ***Analysis of Nuclei Internalisation in Embryos – angle probability distributions from cuts***
638 Embryos expressing H2Av::mCherry were segmented using level sets and watershed algorithms
639 in MATLAB®. Regions of low nuclear density were identified as pixels that were positioned
640 greater than 20% of the average nucleus separation from the nearest nucleus. The centre of mass
641 of the low-density region was identified. The division angle orientation φ of the neighbouring
642 nuclei was measured relative to the centre of mass. Therefore, a nucleus dividing directly into
643 the region of low density would be assigned an angle of 0º, and a nucleus dividing perpendicular
644 to the region would be assigned an angle 90º. As the division does not have a preferred direction,
645 the angle range is between 0º and 90º. A similar analysis was performed for the laser ablations,

where the centre of the low-density region (artificially generated by ablating nuclei) was used to determine the relative angle of the division axis for the neighbouring nuclei.

649 **References**

650 1. Lecuit, T. & Wieschaus, E. Polarized Insertion of New Membrane from a Cytoplasmic
651 Reservoir during Cleavage of the Drosophila Embryo. *J Cell Biol* **150**, 849–860 (2000).

652 2. Foe, V. E., Field, C. M. & Odell, G. M. Microtubules and mitotic cycle phase modulate
653 spatiotemporal distributions of F-actin and myosin II in Drosophila syncytial blastoderm
654 embryos. *Development* **127**, 1767–87 (2000).

655 3. Kanesaki, T., Edwards, C. M., Schwarz, U. S. & Grosshans, J. Dynamic ordering of nuclei
656 in syncytial embryos: a quantitative analysis of the role of cytoskeletal networks. *Integr Biol* **3**,
657 1112–1119 (2011).

658 4. Deneke, V. E., Melbinger, A., Vergassola, M. & Di Talia, S. Waves of Cdk1 Activity in S
659 Phase Synchronize the Cell Cycle in Drosophila Embryos. *Dev Cell* **38**, 399–412 (2016).

660 5. Petkova, M. D., Tkačik, G., Bialek, W., Wieschaus, E. F. & Gregor, T. Optimal Decoding of
661 Cellular Identities in a Genetic Network. *Cell* **176**, 844-855.e15 (2019).

662 6. Dassow, G. von & Schubiger, G. How an actin network might cause fountain streaming and
663 nuclear migration in the syncytial Drosophila embryo. *J Cell Biol* **127**, 1637–1653 (1994).

664 7. Valdés-pérez, R. E. & Minden, J. S. Drosophila melanogaster syncytial nuclear divisions are
665 patterned: time-lapse images, hypothesis and computational evidence. *J Theor Biol* **175**, 525–
666 532 (1995).

667 8. Kaiser, F. *et al.* Mechanical Model of Nuclei Ordering in Drosophila Embryos Reveals
668 Dilution of Stochastic Forces. *Biophys J* **114**, 1730–1740 (2018).

669 9. Deneke, V. E. *et al.* Self-Organized Nuclear Positioning Synchronizes the Cell Cycle in
670 Drosophila Embryos. *Cell* **177**, 925-941.e17 (2019).

671 10. Postner, M. A., Miller, K. G. & Wieschaus, E. F. Maternal effect mutations of the sponge
672 locus affect actin cytoskeletal rearrangements in Drosophila melanogaster embryos. *J Cell Biol*
673 **119**, 1205–1218 (1992).

674 11. Dutta, S., Djabrayan, N. J.-V., Torquato, S., Shvartsman, S. Y. & Krajnc, M. Self-similar
675 dynamics of nuclear packing in the early Drosophila embryo. *Biophys J* **117**, 743–750 (2019).

676 12. Lv, Z. *et al.* The Emergent Yo-yo Movement of Nuclei Driven by Cytoskeletal Remodeling
677 in Pseudo-synchronous Mitotic Cycles. *Curr Biol* **30**, 1–10 (2020).

678 13. Foe, V. E. & Alberts, B. M. Studies of nuclear and cytoplasmic behaviour during the five
679 mitotic cycles that precede gastrulation in Drosophila embryogenesis. *J Cell Sci* **61**, 31–70
680 (1983).

681 14. Krzic, U., Gunther, S., Saunders, T. E., Streichan, S. J. & Hufnagel, L. Multiview light-
682 sheet microscope for rapid in toto imaging. *Nat Methods* **9**, 730–3 (2012).

683 15. Zalokar, M. & Erk, I. Division and migration of nuclei during early embryogenesis of
684 Drosophila melanogaster. *J Microscopie Biol Cell* **25**, 97–106 (1976).

685 16. Hatanaka, K. & Okada, M. Retarded nuclear migration in Drosophila embryos with
686 aberrant F-actin reorganization caused by maternal mutations and by cytochalasin treatment.
687 *Development* **111**, 909–20 (1991).

688 17. Baker, J., Theurkauf, W. & Schubiger, G. Dynamic changes in microtubule configuration
689 correlate with nuclear migration in the preblastoderm Drosophila embryo. *J Cell Biol* **122**,
690 113–121 (1993).

691 18. Callaini, G. & Riparbelli, M. G. Centriole and centrosome cycle in the early Drosophila
692 embryo. *J Cell Sci* **97**, 539–43 (1990).

693 19. Tanimoto, H., Sallé, J., Dodin, L. & Minc, N. Physical forces determining the persistency
694 and centring precision of microtubule asters. *Nat Phys* **14**, 848–854 (2018).

695 20. Mitchison, T. *et al.* Growth, interaction, and positioning of microtubule asters in extremely
696 large vertebrate embryo cells. *Cytoskeleton* **69**, 738–750 (2012).

697 21. Paz, J. & Lüders, J. Microtubule-Organizing Centers: Towards a Minimal Parts List.
698 *Trends Cell Biol* **28**, 176–187 (2018).

699 22. Telley, I. A., Gáspár, I., Ephrussi, A. & Surrey, T. Aster migration determines the length
700 scale of nuclear separation in the Drosophila syncytial embryo. *J Cell Biol* **197**, 887–895
701 (2012).

702 23. Basto, R. *et al.* Flies without Centrioles. *Cell* **125**, 1375–1386 (2006).

703 24. Vaizel-Ohayon, D. & Schejter, E. D. Mutations in centrosomin reveal requirements for
704 centrosomal function during early Drosophila embryogenesis. *Curr Biol* **9**, 889–898 (1999).

705 25. Megraw, T. L., Li, K., Kao, L. R. & Kaufman, T. C. The centrosomin protein is required
706 for centrosome assembly and function during cleavage in Drosophila. *Development* **126**, 2829–
707 39 (1999).

708 26. Telley, I. A., Gáspár, I., Ephrussi, A. & Surrey, T. A single Drosophila embryo extract for
709 the study of mitosis ex vivo. *Nat Protoc* **8**, 310–324 (2013).

710 27. Freeman, M., Nüsslein-Volhard, C. & Glover, D. M. The dissociation of nuclear and
711 centrosomal division in gnu, a mutation causing giant nuclei in Drosophila. *Cell* **46**, 457–468
712 (1986).

713 28. Lee, L. A., Hoewyk, D. V. & Orr-Weaver, T. L. The Drosophila cell cycle kinase PAN GU
714 forms an active complex with PLUTONIUM and GNU to regulate embryonic divisions. *Gene*
715 *Dev* **17**, 2979–2991 (2003).

716 29. Grill, S. W., Howard, J., Schäffer, E., Stelzer, E. H. K. & Hyman, A. A. The Distribution of
717 Active Force Generators Controls Mitotic Spindle Position. *Science* **301**, 518–521 (2003).

718 30. Wühr, M., Dumont, S., Groen, A. C., Needleman, D. J. & Mitchison, T. J. How does a
719 millimeter-sized cell find its center? *Cell Cycle* **8**, 1115–1121 (2009).

720 31. Bak, P., Tang, C. & Wiesenfeld, K. Self-organized criticality: An explanation of the 1/ f
721 noise. *Phys Rev Lett* **59**, 381–384 (1987).

722 32. Hughes, D. & Paczuski, M. Large Scale Structures, Symmetry, and Universality in
723 Sandpiles. *Phys Rev Lett* **88**, 054302 (2001).

724 33. Gennes, P. G. de, Prost, J. & Pelcovits, R. The Physics of Liquid Crystals. *Phys Today* **48**,
725 70–71 (1995).

726 34. Chakraborty, A. & Manna, S. S. Space-filling Percolation. *Phys Rev E* **89**, 032103 (2014).

727 35. Jo, W. S., Yi, S. D., Baek, S. K. & Kim, B. J. Cluster-size heterogeneity in the two-
728 dimensional Ising model. *Phys Rev E* **86**, 032103 (2012).

729 36. Moessner, R. & Chalker, J. T. Properties of a Classical Spin Liquid: The Heisenberg
730 Pyrochlore Antiferromagnet. *Phys Rev Lett* **80**, 2929–2932 (1998).

731 37. Freeman, M. & Glover, D. M. The gnu mutation of Drosophila causes inappropriate DNA
732 synthesis in unfertilized and fertilized eggs. *Gene Dev* **1**, 924–930 (1987).

733 38. Holy, T. E., Dogterom, M., Yurke, B. & Leibler, S. Assembly and positioning of
734 microtubule asters in microfabricated chambers. *PNAS* **94**, 6228–6231 (1997).

735 39. Dogterom, M. & Yurke, B. Measurement of the Force-Velocity Relation for Growing
736 Microtubules. *Science* **278**, 856–860 (1997).

737 40. Bieling, P., Telley, I. A. & Surrey, T. A Minimal Midzone Protein Module Controls
738 Formation and Length of Antiparallel Microtubule Overlaps. *Cell* **142**, 420–432 (2010).

739 41. Subramanian, R., Ti, S.-C., Tan, L., Darst, S. A. & Kapoor, T. M. Marking and Measuring
740 Single Microtubules by PRC1 and Kinesin-4. *Cell* **154**, 377–390 (2013).

741 42. Jeune-Smith, Y. & Hess, H. Engineering the length distribution of microtubules
742 polymerized in vitro. *Soft Matter* **6**, 1778–1784 (2010).

743 43. Howard, J. *Mechanics of motor proteins and cytoskeleton*. (Sinauer Associates), 2001,
744 ISBN 978-0878933334.

745 44. Forth, S., Hsia, K.-C., Shimamoto, Y. & Kapoor, T. M. Asymmetric Friction of Nonmotor
746 MAPs Can Lead to Their Directional Motion in Active Microtubule Networks. *Cell* **157**, 420–
747 432 (2014).

748 45. Laan, L. *et al.* Cortical dynein controls microtubule dynamics to generate pulling forces
749 that position microtubule asters. *Cell* **148**, 502–14 (2012).

750 46. Zhu, J., Burakov, A., Rodionov, V. & Mogilner, A. Finding the cell center by a balance of
751 dynein and myosin pulling and microtubule pushing: a computational study. *Mol Biol Cell* **21**,
752 4418–27 (2010).

753 47. Kinneret, K. Non Equilibrium Steady State Dynamics of Contractile Actin Networks.
754 *Biophys J* **110**, 174a (2016).

755 48. Rogers, S. L., Rogers, G. C., Sharp, D. J. & Vale, R. D. Drosophila EB1 is important for
756 proper assembly, dynamics, and positioning of the mitotic spindle. *J Cell Biol* **158**, 873–884
757 (2002).

758 49. Robinson, J. T., Wojcik, E. J., Sanders, M. A., McGrail, M. & Hays, T. S. Cytoplasmic
759 Dynein Is Required for the Nuclear Attachment and Migration of Centrosomes during Mitosis
760 in Drosophila. *J Cell Biol* **146**, 597–608 (1999).

761 50. Nestor-Bergmann, A., Goddard, G. & Woolner, S. Force and the spindle: mechanical cues
762 in mitotic spindle orientation. *Semin Cell Dev Biol* **34**, 133–9 (2014).

763 51. Inoue, Y. H. *et al.* Mutations in orbit/mast reveal that the central spindle is comprised of
764 two microtubule populations, those that initiate cleavage and those that propagate furrow
765 ingression. *J Cell Biol* **166**, 49–60 (2004).

766 52. Schubiger, G. & Edgar, B. Using inhibitors to study embryogenesis. *Methods Cell Biol* **44**,
767 697–713 (1994).

768 53. de-Carvalho, J., Deshpande, O., Nabais, C. & Telley, I. A. A cell-free system of Drosophila
769 egg explants supporting native mitotic cycles. *Methods Cell Biol* **144**, 233–257 (2018).

770 54. Tinevez, J.-Y. *et al.* TrackMate: An open and extensible platform for single-particle
771 tracking. *Methods* **115**, 80–90 (2016).

772 55. Schindelin, J. *et al.* Fiji: an open-source platform for biological-image analysis. *Nat*
773 *Methods* **9**, 676–682 (2012).

774 56. Saw, T. B. *et al.* Topological defects in epithelia govern cell death and extrusion. *Nature*
775 **544**, 212–216 (2017).

776 57. Menzel, A. M. & Ohta, T. Soft deformable self-propelled particles. *EPL* **99**, 58001 (2012).

777
778

Supplementary Figures

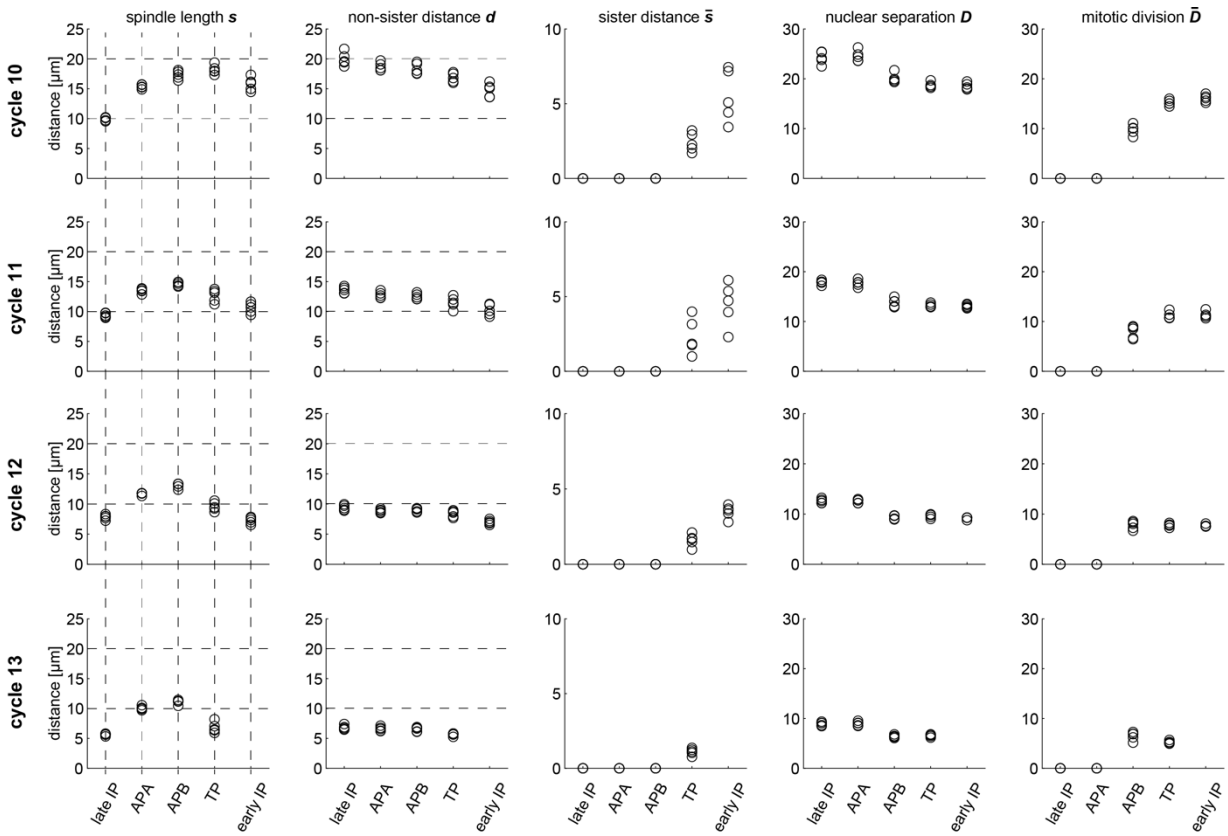

Supplementary Fig. 1 – Timeline of average inter-nuclear and inter-aster distances. Averages from five blastoderm embryos during cycles 10, 11, 12 and 13. Each cycle is characterised by late interphase (late IP), anaphase A (APA), anaphase B (APB), telophase (TP) and early interphase (early IP). Morphological criteria for identification of mitotic phases and hierarchical classification of distances; *Nuclear-based*: D – non-sister nuclei identified as nearest neighbours. $\overline{D}$ – sister chromatids/nuclei. *Aster-based*: s – sister asters ~ spindle length. $\bar{s}$ – sisters in the following mitotic cycle, i.e, s becomes $\bar{s}$ after early interphase of the ensuing mitotic cycle. d – non-sister asters identified as nearest neighbours (distribution data from cycle 10 is presented in Fig. 1, details on the measurements in Methods).

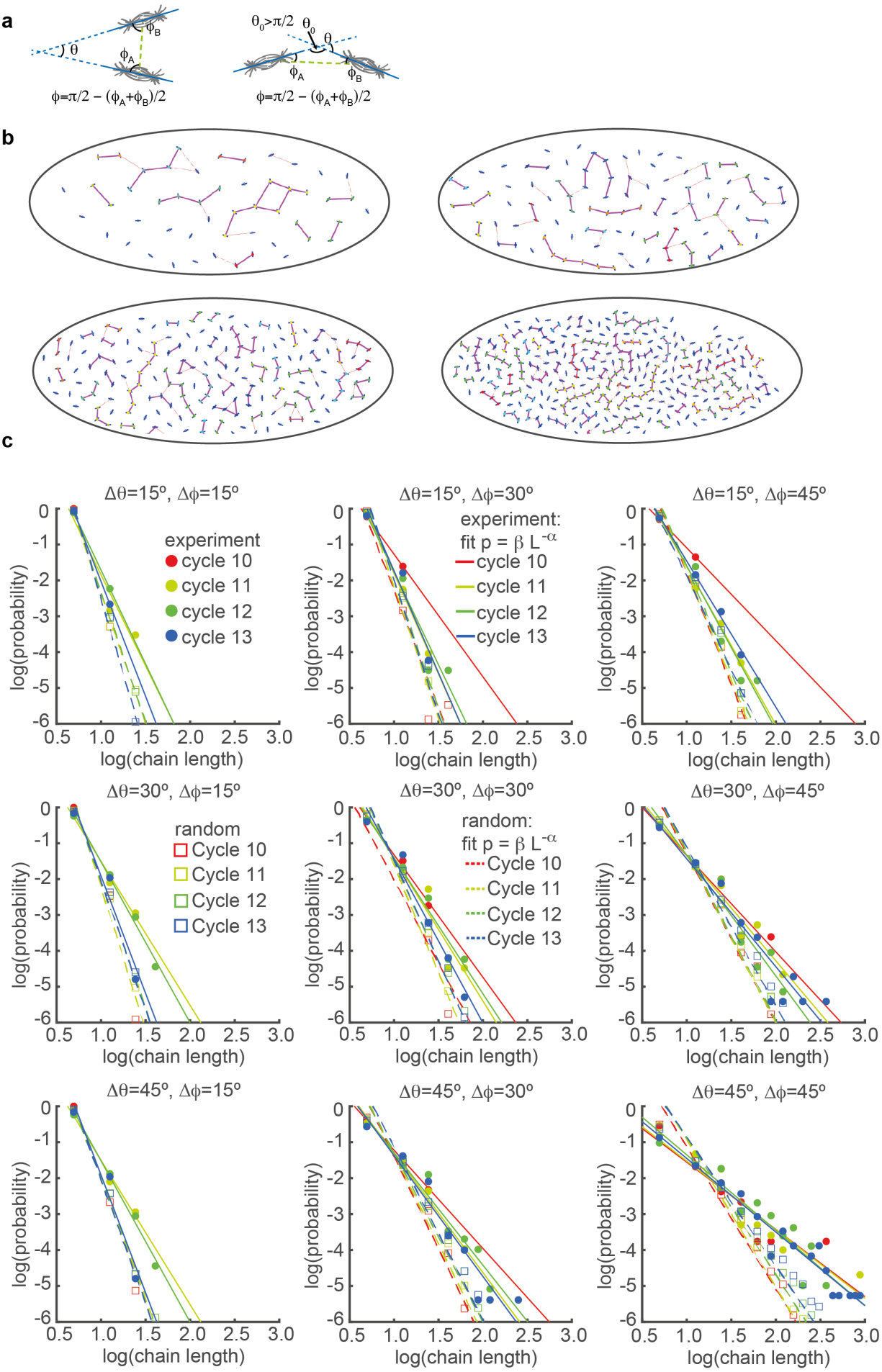
a
θ
ϕ_A
ϕ_B
$\phi=\pi/2-(\phi_A+\phi_B)/2$
$\theta_0>\pi/2$
θ_0
θ
ϕ_A
ϕ_B
$\phi=\pi/2-(\phi_A+\phi_B)/2$
b
c
Δθ=15°, Δϕ=15°
Δθ=15°, Δϕ=30°
Δθ=15°, Δϕ=45°
Δθ=30°, Δϕ=15°
Δθ=30°, Δϕ=30°
Δθ=30°, Δϕ=45°
Δθ=45°, Δϕ=15°
Δθ=45°, Δϕ=30°
Δθ=45°, Δϕ=45°
experiment
cycle 10
cycle 11
cycle 12
cycle 13
experiment:
fit $p = \beta L^{-\alpha}$
random
Cycle 10
Cycle 11
Cycle 12
Cycle 13
random:
log(probability)
log(chain length)
0
-1
-2
-3
-4
-5
-6
0.5
1.0
1.5
2.0
2.5
3.0

Supplementary Fig. 2 – Scaling of chain length probability with chain length for different inclusion criteria. (a) Schematic of geometric considerations in 2D of neighbour spindle alignment. Spindle axes are in cyan. Left shows almost parallel division axes (θ small), orientated perpendicular to the vector between the two spindles (ϕ almost 90º). Right shows almost colinear alignment (θ small, ϕ small). The spindle does not have a specific vector direction, so angles are between 0º and 90º. A chain is defined by spindles fulfilling one or two of the following conditions; (i) $0 \leq \theta \leq \Delta\theta$ (ii) $\Delta\phi \leq \phi \leq 90°$ (Methods). **(b)** Representative embryo in n.c. 10, 11, 12 and 13 showing alignment chains. Solid purple lines denote nearest neighbours that satisfy the two chain conditions with angles $\Delta\phi = 45°$ and $\Delta\theta = 45°$. Thin dashed red lines denote nearest neighbours that satisfy only chain condition (i). **(c)** Logarithmic plots of probability as a function of chain length for different chain conditions. Filled symbols denote experimental data and open symbols are from simulations of randomised orientations. Lines represent a fit to $\beta C^{-\alpha}$, where C is the chain length and α is the scaling exponent (fitting performed with *fit* in MATLAB®); solid lines are fits to experimental data and dashed lines are fits to simulated data of randomised orientations. We generated 1000 random orientations for each embryo at each cycle.

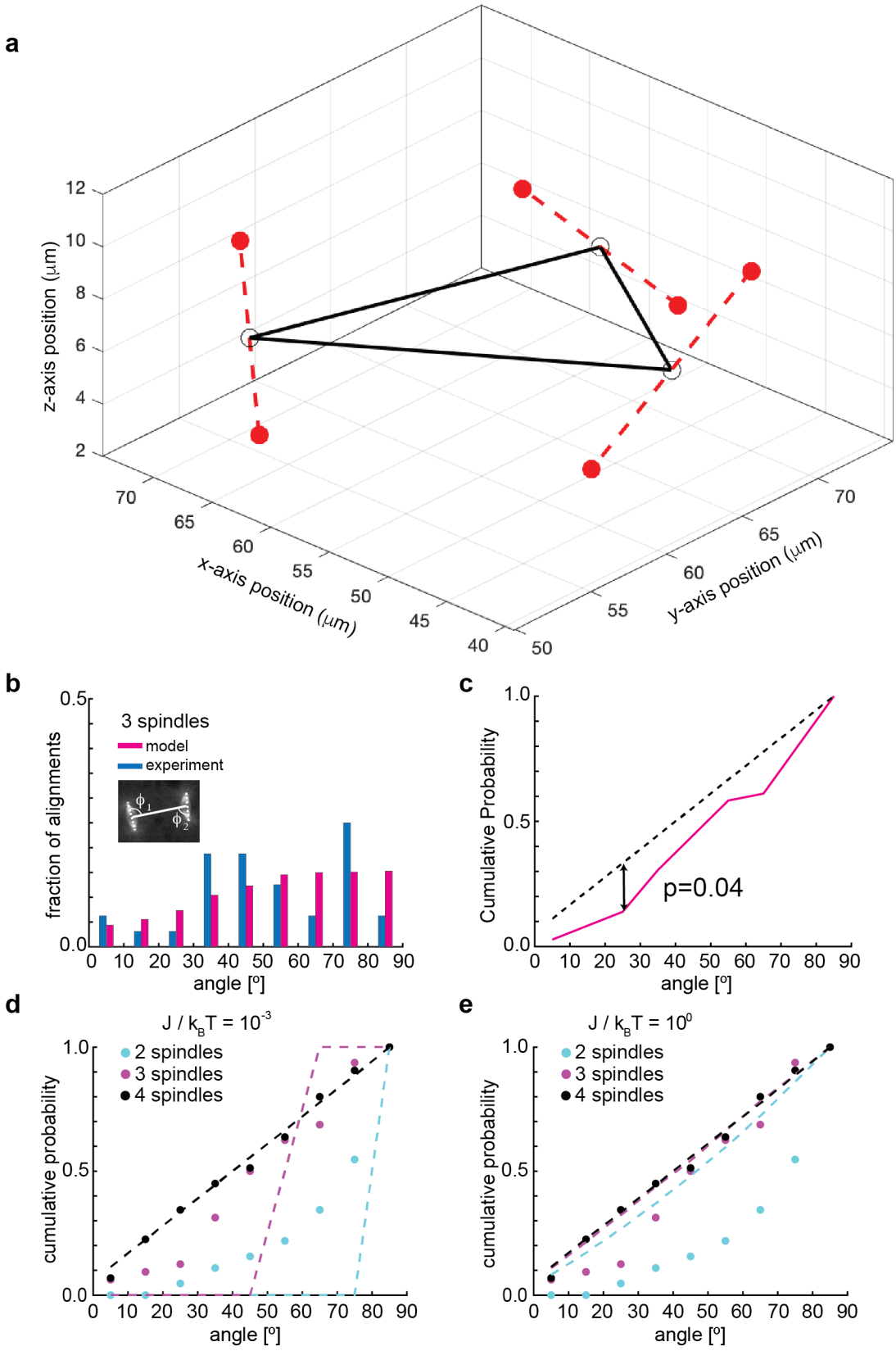

Supplementary Fig. 3 – Division orientation of three spindles in a cytosolic explant, and influence of effective temperature. (a) 3D plot of the shortest distance (black solid line) between three spindle centres (open circles). The spindle orientations (dashed lines) and positions of associated asters (filled circles) illustrate the adjustment of orientation and position

in this simple system. **(b)** Histogram of the angle ϕ between spindle axis and the connecting line (inset) for the three-spindle scenario from experimental (blue, n=7) and *in silico* (magenta) data ($J/k_BT = 10^{-1}$). **(c)** Cumulative probability of relative division axis for the 3-spindle scenario and randomised orientation. p-value was determined from Kolmogorov–Smirnov test. **(d, e)** Cumulative probabilities of spindle axes orientation for two-, three- and four-spindle scenarios at different effective simulation temperature. Dashed lines are model predictions with either low (**d**) or high (**e**) effective temperature (thermal noise).

Explant

a Steady-state distance between the two asters

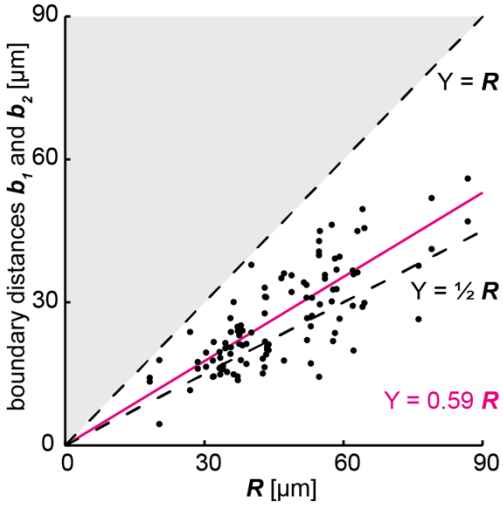

b Boundary distance of each asters in a two-aster scenario

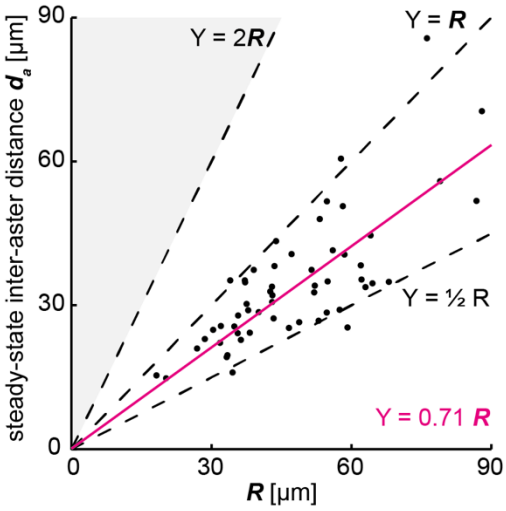

c Boundary distances in the two-aster scenario

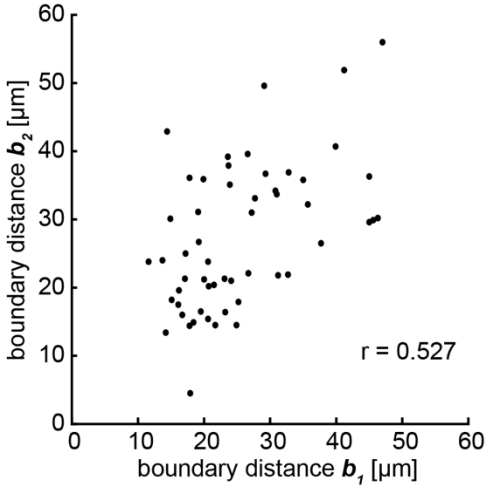

Embryo

d Aster positioning in the *gnu* mutant embryo

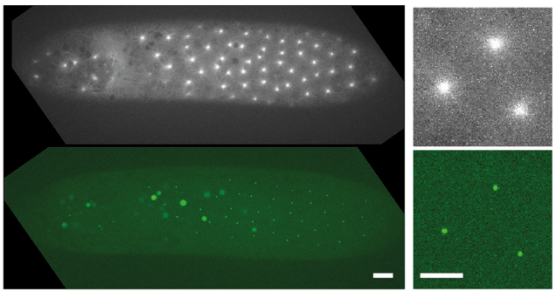

e Steady state inter-aster distance in the *gnu* embryo

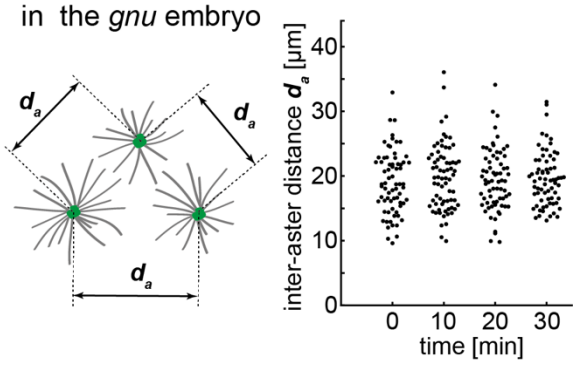

Supplementary Figure 4 – Distance analysis of asters in explants and embryos in the absence of nuclei. (a) Scatter plot of shortest distance to explant boundary (b_1 and b_2) as a function of the radius R in explants containing two asters (n=54; details in inset of Fig. 3d). The magenta line represents the linear regression. Black dashed lines represent half and full radius distance. **(b)** Scattered plot of inter-aster distance (d_a) as a function of the radius (R) of explants containing two asters (n=54). Most measured data points fall between the dashed lines denoting the explant radius ($Y = R$) and half of the radius ($Y = \frac{1}{2}R$). The magenta line represents the linear regression. **(c)** Correlation plot of the boundary distances b_1 and b_2 referred to in panel (**a**) with Pearson's correlation coefficient *r*. **(d)** Maximum intensity Z-projection of a *gnu* mutant embryo expressing RFP::β-Tubulin (grey) and Spd2::GFP (green) (left, scale bar 20 µm), with magnification of three asters (right, scale bar 10 µm). **(e)** Schematic of the measurement of inter-aster distance d between nearest neighbour asters (left), and scatter plots of d_a during consecutive intervals of 10 min for the same embryo.

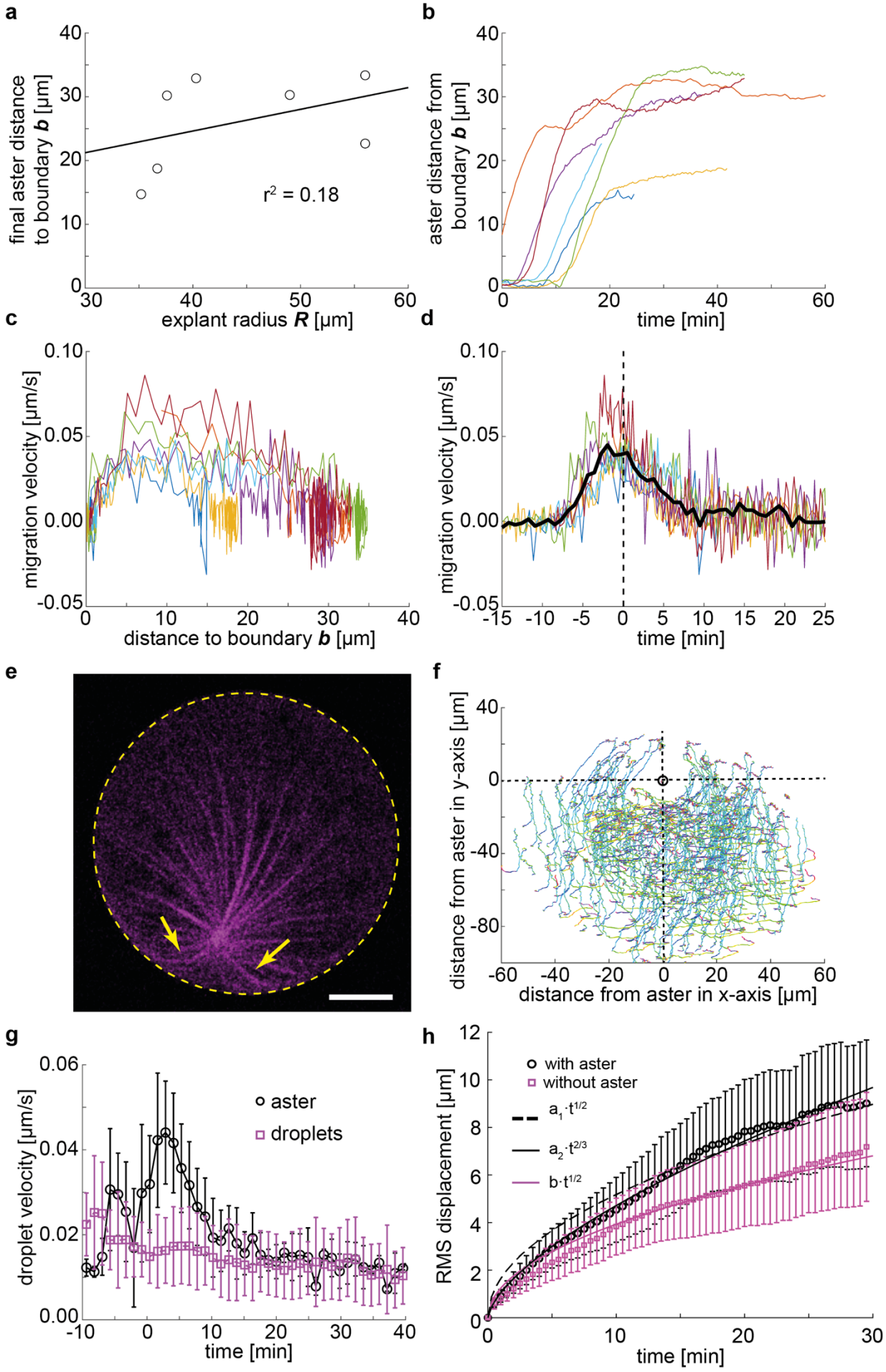
a
final aster distance to boundary b [µm]
explant radius R [µm]
r² = 0.18
b
aster distance from boundary b [µm]
time [min]
c
migration velocity [µm/s]
distance to boundary b [µm]
d
migration velocity [µm/s]
time [min]
e
f
distance from aster in y-axis [µm]
distance from aster in x-axis [µm]
g
droplet velocity [µm/s]
aster
droplets
time [min]
h
RMS displacement [µm]
with aster
without aster
a1·t^1/2
a2·t^2/3
b·t^1/2
time [min]

833

Supplementary Figure 5 – Analysis of migration dynamics in explants containing a single aster. (a) Correlation between explant radius R and final aster distance to the explant boundary after reaching a steady state (n=7 for **a-d**). The solid line represents the linear regression to experimental data. **(b)** Trajectories of normalised aster distance to the explant boundary from independent experiments. **(c)** Migration velocity as a function of boundary distance. **(d)** Aster separation velocity as a function of time, where t=0 is defined as the time when the aster lies midway between the explant edge and the final position of the aster. Solid line represents average over all measurements. **(e)** Z-projection of a 3D image stack of a small explant containing one aster that exemplifies microtubule buckling and splay near the explant boundary (scale bar 5 µm). **(f)** Velocity field of yolk droplets around the single aster as it escapes from the explant boundary. Image rotation and frame matching were performed to overlay all experiments such that the aster, at each time point is positioned at (0,0) and moves in the direction (0,-1). Track colour coding denotes displacement angle, where turquoise corresponds to 0° and red to 90°. **(g)** Velocity profile of asters (black) and 35 lipid droplet (magenta) tracks within a distance of 20 µm from the aster, where t=0 is the time point at which the aster starts moving away from the explant boundary. **(h)** Root-mean-square (RMS) displacement of lipid droplets in the explants. Droplet movement analysed with (black) and without (magenta, n=6) an aster. Error bars s.e.m. and lines represent fits to models shown in legend. Measurements in explants with aster fit best to a model exhibiting some directionality, see Methods for further discussion.

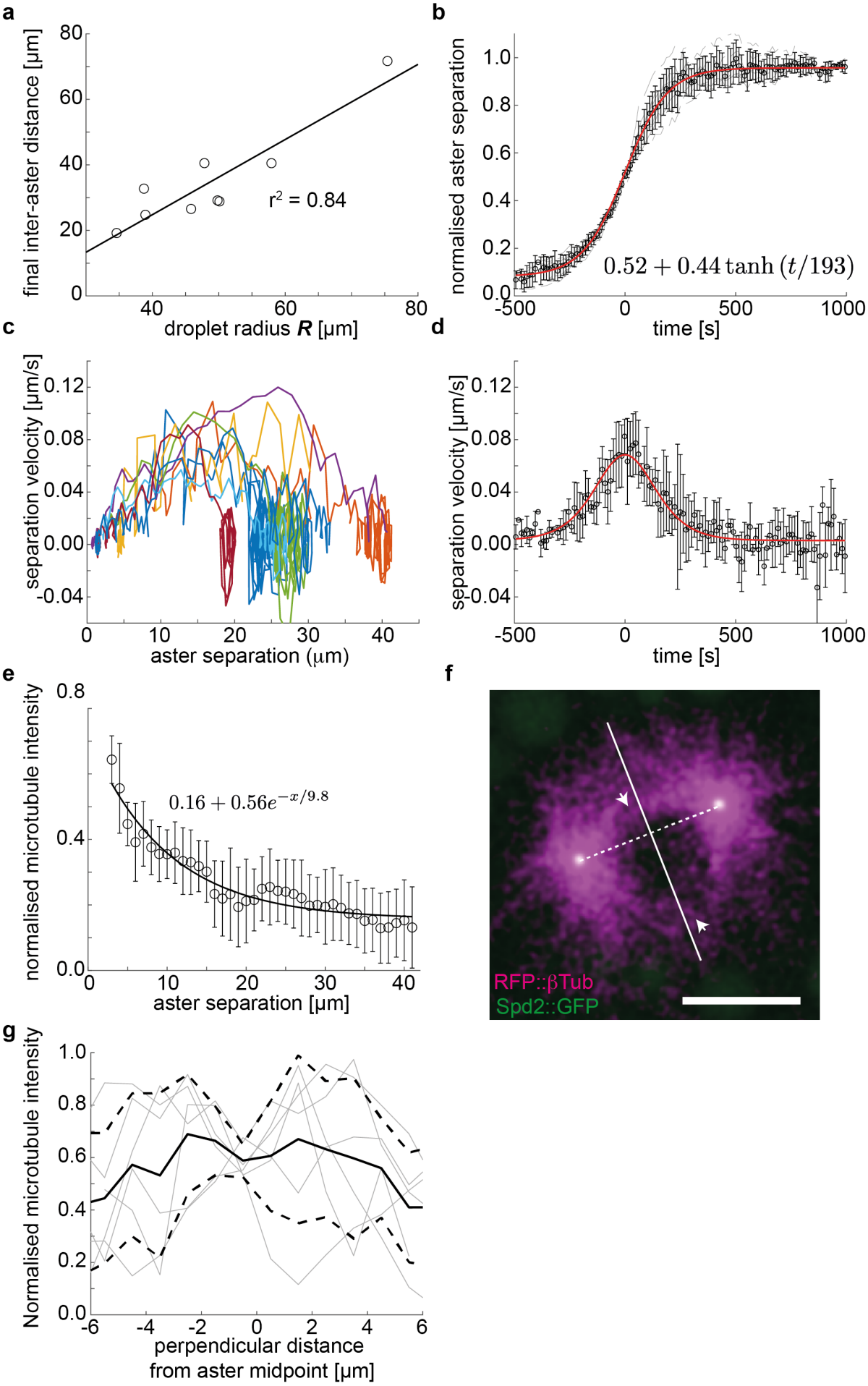
a
final inter-aster distance [μm]
droplet radius R [μm]
r² = 0.84
b
normalised aster separation
time [s]
0.52 + 0.44 tanh (t/193)
c
separation velocity [μm/s]
aster separation (μm)
d
separation velocity [μm/s]
time [s]
e
normalised microtubule intensity
aster separation [μm]
0.16 + 0.56e^{−x/9.8}
f
RFP::βTub
Spd2::GFP
g
Normalised microtubule intensity
perpendicular distance
from aster midpoint [μm]

854 **Supplementary Figure 6 – Analysis of separation dynamics in explants containing two**
855 **asters. (a)** Correlation between explant radius *R* and the final distance between asters after
856 reaching a steady state (n=9). The solid line represents the linear regression to experimental data.
857 **(b)** Normalised aster separation distance versus time, where t=0 is defined as the time when the
858 aster lies midway between the explant edge and the final position of the aster. Solid line
859 represents the fit to a hyperbolic tangent function (n=9). **(c)** Aster separation velocity as a
860 function of aster separation, as defined above. Each colour corresponds to a different experiment
861 (n=8). **(d)** Aster separation velocity versus time, where t=0 is defined as above. Solid line denotes
862 the fitting to the time derivative of the *tanh* function shown in (**b**) (n=9). **(e)** Normalised
863 microtubule intensity at the midpoint perpendicular axis between asters in function of aster
864 separation distance. Open markers denote average values and error bars the standard deviation.
865 Solid line represents the fitting to exponential decay (n=7), fitting performed using MATLAB
866 *fit* function. **(f)** Two colour maximum intensity Z-projection of two separating asters in an
867 explant with fluorescent reporters for Spd2::GFP (green) and RFP::β-Tubulin (magenta). A void
868 of microtubules in the centre between two separating asters is observed during the initial
869 acceleration phase. Scale bar, 10 μm. **(g)** Normalised microtubule intensity along the
870 perpendicular midpoint axis of separating aster during the initial acceleration phase. Solid line
871 denotes average normalised (for each experiment, as discussed in Methods) microtubule density
872 and dashed lines ±1s.d. (n=6). There was significant variation between samples and the
873 microtubule signal was often weak, making a detailed analysis challenging.

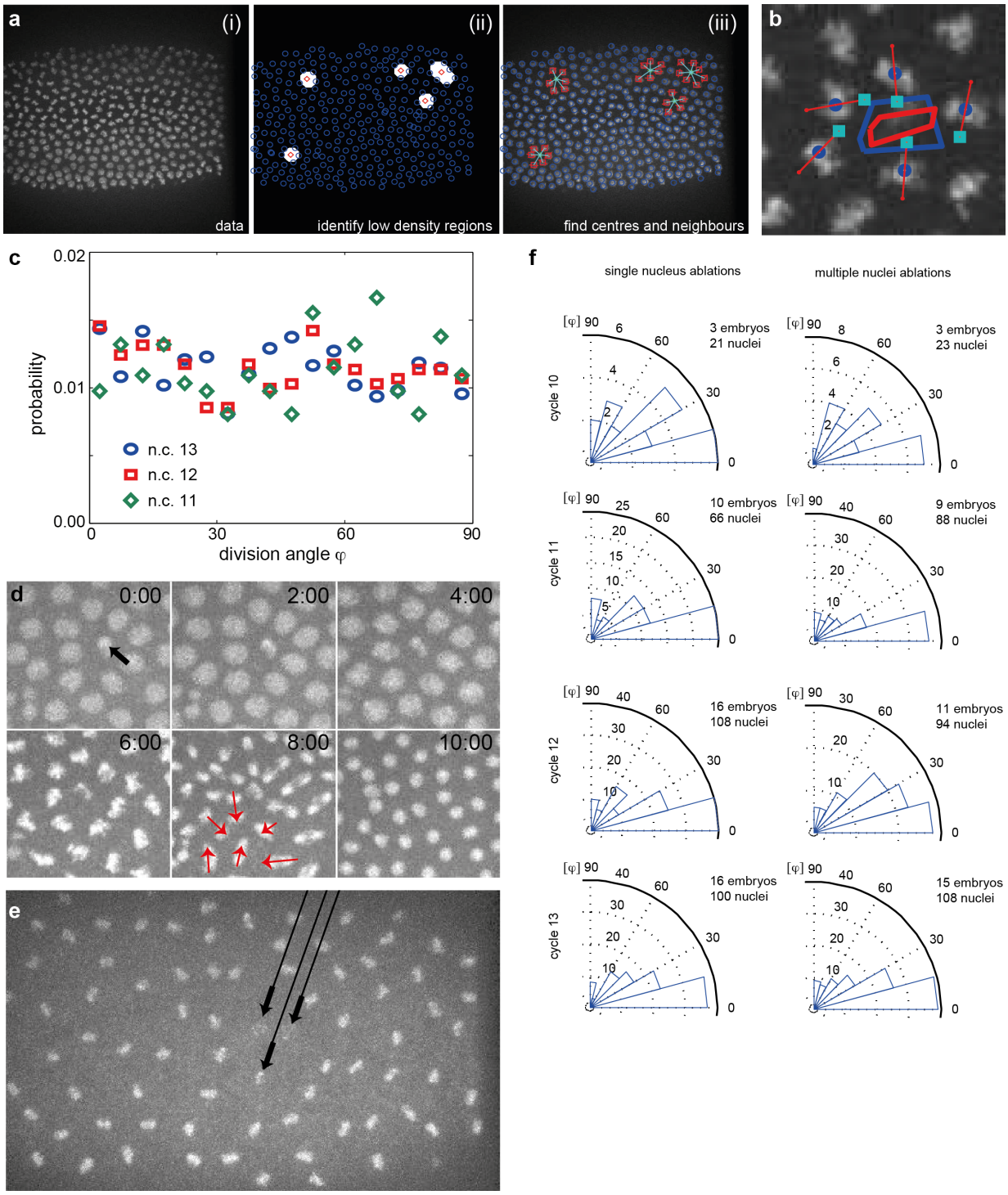

Supplementary Figure 7 – Analysis of nuclei division orientation *in vivo*

(a) (i) Embryo expressing H2Av::mCherry just prior to anaphase B of n.c. 13 . (ii) Areas of low nuclear density were identified by finding pixels with no nuclei within 20% of the average nuclear separation and the centroid of these areas found (red diamonds). (iii) The nuclei (red squares) neighbouring the low density region were then identified. **(b)** Examples of nuclear division near a region of low nuclear density. The division axis orientation of the neighbouring nuclei to a region of low density was measured (red bars) and the subsequent position of the

882 nuclei after division identified (turquoise squares). Change in area of low nuclear density region
883 from before (blue) to after (red) area is shown. **(c)** Analysis performed as in Fig. 5g, but for
884 arbitrary locations selected within the embryo. **(d)** Artificial generation of a region of low nuclear
885 density by ablating a nucleus (Methods). Black arrow in top left panel identifies ablated nucleus;
886 ablation at time t=0 min. Images from maximum intensity projection of embryo expressing
887 H2Av::mCherry. Red arrows at 8 min denote division axis orientation of neighbouring nuclei to
888 the ablated nucleus. **(e)** Similar to (**d**), except three nuclei are ablated to generate a larger region
889 of low nuclear density. **(f)** Rose plots of division axis orientation for nuclei adjacent to ablated
890 nuclei, for single (left column) and multi-nuclei (right column) ablations.

891 **Supplementary Video Legends**

892 **Supp. Video 1:** Maximum intensity Z-projection from a 3D time-lapse movie of an embryo
893 expressing H2Av::RFP (magenta) and Spd2::GFP (green) from interphase of n.c. 10 until the
894 end of n.c. 13 (time in min:sec, scale bar 20 µm). In support of Fig. 1.

895 **Supp. Video 2:** Maximum intensity Z-projection from a 3D time-lapse movies of three distinct
896 cycling explants starting with a single spindle extracted from embryos expressing Jupiter::GFP
897 (grey) and H2Av::RFP (magenta) (time in min:sec, scale bar 10 µm). In support of Fig. 2.

898 **Supp. Video 3:** Maximum intensity Z-projection from a 3D time-lapse movie of a *gnu* mutant
899 embryo, approximately 1h old embryo expressing β-Tubulin::EGFP (grey) (time in hr:min:sec,
900 scale bar 10 µm). In support of Fig. 3.

901 **Supp. Video 4:** Maximum intensity Z-projection from a 3D time-lapse movie of an explant
902 generated from a *gnu* mutant embryo expressing RFP::β-Tubulin (magenta) and Spd2::GFP
903 (green), containing a single aster moving away from the explant boundary (time in min:sec, scale
904 bar 10 µm). In support of Fig. 3 and 4.

905 **Supp. Video 5:** Maximum intensity Z-projection from a 3D time-lapse movie of a *gnu* mutant
906 embryo, approximately 4h old embryo expressing β-Tubulin::GFP (grey) (time in min:sec, scale
907 bar 10 µm). In support of Fig. 3.

908 **Supp. Video 6:** Maximum intensity Z-projection from a 3D time-lapse movie of an explant
909 generated from a *gnu* mutant embryo expressing RFP::β-Tubulin (magenta) and Spd2::GFP
910 (green), containing two separating asters (time in min:sec, scale bar 10 µm). In support of Fig.
911 4.

912 **Supp. Video 7:** Maximum intensity Z-projection from a 3D time-lapse movie of explants
913 generated from a *gnu* mutant embryo expressing RFP::β-Tubulin (magenta) and Spd2::GFP
914 (green), containing two separating asters, after pulse injection of solutions: control with buffer
915 (left), 10 mM sodium azide (centre) and 0.2 mM of colchicine (time in min:sec, scale bar 10
916 µm). In support of Fig. 4.

917 **Supp. Video 8:** Maximum intensity Z-projection from a 3D time-lapse movie of explants
918 generated from a *gnu* mutant embryo expressing RFP::β-Tubulin (magenta) and Spd2::GFP
919 (green) containing a single aster (time in min:sec, scale bar 10 µm). The aster was allowed to
920 equilibrate followed by an asymmetric elliptic ablation (yellow line at times 00:15 to 01:00)
921 performed in control explants (no injection) and in explants supplemented with 0.2mM of
922 colchicine. In support of Fig. 5.

923 **Supp. Video 9:** Maximum intensity Z-projection from a 3D time-lapse movie of an explant
924 containing two separating asters from a *gnu* mutant embryo expressing RFP::β-Tubulin
925 (magenta) and Spd2::GFP (green) (time in min:sec, scale bar 10 µm). The elliptic ablation
926 (yellow line from 00:15 to 00:45) was performed when asters were ~7 µm apart. In support of
927 Fig. 5.

928 **Supp. Video 10:** Maximum intensity Z-projection from a 3D time-lapse movie of a wildtype
929 embryo expressing H2Av::mCherry (magenta) and Spd2::GFP (green) during n.c. 12 and 13, in
930 response to spontaneous nuclear internalisation (time in min:sec, scale bar 20 µm). In support of
931 Fig. 5.